Ezrin defines TSC complex activation at endosomal compartments through EGFR-AKT signaling.

Giuliana Giamundo[1#], Daniela Intartaglia[1#], Eugenio Del Prete[2], Elena Polishchuk[2], Fabrizio Andreone[2], Marzia Ognibene[3], Sara Buonocore[1], Bruno Hay Mele[1], Francesco Giuseppe Salierno[2], Jlenia Monfregola[2], Dario Antonini[1], Paolo Grumati[2,4], Alessandra Eva[5], Rossella de Cegli[2], Ivan Conte[1]*

1. Department of Biology, University of Naples Federico II, Strada Vicinale Cupa Cintia, 21, Naples 80126 Italy
2. Telethon Institute of Genetics and Medicine, Via Campi Flegrei 34, Pozzuoli (Naples), 80078, Italy.
3. U.O.C. Genetica Medica, IRCCS Istituto Giannina Gaslini, 16147, Genova, Italy
4. Clinical Medicine and Surgery, University of Naples Federico II, Via S. Pansini 5, 80131 Naples Italy.
5. Laboratory of Molecular Biology, IRCCS Istituto Giannina Gaslini, Genova, Italy.

#These authors contributed equally to this work

* Corresponding author

ivan.conte@unina.it

Abstract

Endosomes have emerged as major signaling hubs where different internalized ligand-receptor complexes are integrated and the outcome of signaling pathways are organized to regulate the strength and specificity of signal transduction events. Ezrin, a major membrane-actin linker that assembles and coordinates macromolecular signaling complexes at membranes, has emerged recently as an important regulator of lysosomal function. Here, we report that endosomal-localized EGFR/Ezrin complex interacts with and triggers the inhibition of the Tuberous Sclerosis Complex (TSC complex) in response to EGF stimuli. This is regulated through activation of the AKT signaling pathway. Loss of Ezrin was not sufficient to repress TSC complex by EGF and culminated in translocation of TSC complex to lysosomes triggering suppression of mTORC1 signaling. Overexpression of constitutively active EZRIN^{T567D} is sufficient to relocalize TSC complex to the endosomes and reactivate mTORC1. Our findings identify EZRIN as a critical regulator of autophagy via TSC complex in response to EGF stimuli and establish the central role of early endosomal signaling in the regulation of mTORC1. Consistently, Medaka fish deficient for Ezrin exhibit defective endo-lysosomal pathway, attributable to the compromised EGFR/AKT signaling, ultimately leading to retinal degeneration. Our data identify a pivotal mechanism of endo-lysosomal signaling involving Ezrin and its associated EGFR/TSC complex, which are essential for retinal function.

Keywords: EGFR, EZRIN, endosomal signaling, TSC complex, mTORC1.

Abbreviations: RPE: retinal pigment epithelium; POS: photoreceptor outer segment; ERM: Ezrin-radix-moesin; EZR: Ezrin; NHE1: sodium-hydrogen antiporter 1; EGFR: epidermal growth factor receptor; Vsp11: vacuolar protein sorting 11; PI3K: Phosphoinositide-3-kinase; AKT: protein kinase B; EGF: epidermal growth factor; TSC complex: Tuberous sclerosis complex; mTORC1: mammalian target of rapamycin complex 1; GTPase: Guanine nucleotide-binding proteins; MEF: Mouse Primary Embryonic Fibroblasts; LAMP1: Lysosomal Associated Membrane Protein 1; LC3: Microtubule-associated proteins 1A/1B light chain 3B; CTSB: Cathepsin B; HER3: human epidermal growth factor receptor 3; HER2: human epidermal growth factor receptor 2; EEA1: early endosome antigen 1; MAPK: mitogen-activated protein kinase; MK2: Mitogen-activated protein kinase-activated protein kinase 2; ARPE: Retinal Pigment Epithelial Cells.

INTRODUCTION

Endosomes are intracellular membrane-bound organelles that receive, integrate, and transmit a variety of signals to intracellular compartments. Trafficking of receptors, ion channels, lipids, and other effector proteins within the endosomal vesicles provides a mechanism to either sustain intracellular signaling pathways active (Palfy, Remenyi, & Korcsmaros, 2012) or to downregulate signaling pathways through their degradation in lysosomes. Accordingly, altered endosomal maturation and function play a key role in the pathogenesis of a wide range of human diseases including diabetes, cancer, and neurodegenerative disorders. Therefore, new insights about endosomal signaling and understanding the molecular components restricting signaling activity to specific pathways will uncover new opportunities for pharmacological targeting of such disorders. In the retinal pigment epithelium (RPE), endosomes contribute to the diurnal clearance of phagocytosed photoreceptor outer segments (POS) that is required for RPE and photoreceptor health. This process is linked to circadian and light phase and is initiated by the scission from the plasma membrane of phagosomes containing

POS, which undergo gradual fusion with endosomes and finally with lysosomes in a coordinated process termed “maturation”. The high demand on lysosomes for the digestion and recycling of phagocytosed POS rather than for the clearance of mitochondria, oxidized proteins, and other cellular components suggests the existence of a signaling pathway that can finely coordinate lysosomal function according to needs that will not upset cellular homeostasis. A long-standing question in the field is how functional diversity within the autophagy pathway is achieved in the RPE in the dark and light phases. Inhibition of endosomal biogenesis, trafficking, and fusion is associated with impairment of lysosomal biogenesis and autophagy flux. Implicit in these findings is the idea that endosomes, by carrying signaling molecules, could serve as a signaling hub for the regulated transfer of signals to lysosomes, acting more specifically than diffusion-based signal propagation. However, how endosomes are essential for lysosomal function, and their relevant components regulating this process are still not well defined.

Ezrin, a member of the ezrin-radixin-moesin (ERM) protein family, is mainly localized just beneath the plasma membrane around cellular protrusions and villi. Ezrin acts as a scaffolding platform to cross-link F-actin cytoskeleton with specialized membrane components (Kawaguchi & Asano, 2022) that are implicated in the spatiotemporal dynamics of phagosomes and endosomes. Its association with both F-actin filaments and membrane proteins is finely regulated and requires conformational activation through phosphorylation at unique (Y353, Y477, and T567) residues. The central role of Ezrin in regulating trafficking of vesicles has been described (Cha et al., 2006; Tamma et al., 2005; Zhou et al., 2003). Indeed, maturation of endosomes and recycling/exocytosis of their components (i.e. α1β-adrenergic receptor, NHE3, and others) require the Ezrin protein (Barroso-Gonzalez, Machado, Garcia-Exposito, & Valenzuela-Fernandez, 2009; Cha et al., 2006; Stanasila, Abuin, Diviani, & Cotecchia, 2006; Zhao et al., 2004; Zhou et al., 2005). The phosphorylated active Ezrin is observed within early and late endosomes (Parameswaran, Enyindah-Asonye, Bagheri, Shah, & Gupta, 2013). Moreover,

through its active and reversible interactions with actin filaments and endosomal proteins, Ezrin organizes signal transduction. Indeed, phosphorylation of the T567 residue of EZRIN leads to its colocalization in a functional complex with NHE1, EGFR, and β1-integrin in human breast tumors, suggesting its crucial role as a scaffold protein of EGFR (Antelmi et al., 2013). Accordingly, Ezrin also interacts with EGFR at membranes (Saygideger-Kont et al., 2016). In mammalian cells, depletion of an Ezrin-interacting protein, Vsp11, delays the delivery of EGFR to endosomes (Chirivino et al., 2011), thus linking the Ezrin protein network with EGFR trafficking via clathrin-coated transport vesicles. However, the mechanisms of Ezrin-EGFR interaction and its function at the endosomal compartments remain largely unexplored. Interestingly, recent findings have shown that PI3K-mediated activation of AKT upon EGF stimulation is mediated by EGFR via an early endocytic pathway (Nishimura, Takiguchi, Ito, & Itoh, 2015). These findings suggest that Ezrin may be required as a protein scaffold for coordinating EGFR/AKT signaling at endosomes. Interestingly, EZR interacts with AKT in breast cancer cells (Li et al., 2019). In addition, the Y353-phosphorylation of Ezrin is relevant for PI3K-initiated signaling through its interaction with p85, the regulatory subunit of PI3K (Gautreau, Poullet, Louvard, & Arpin, 1999). Notably, the Ezrin-p85 complex optimizes the physiological activation of AKT, supporting a central role of Ezrin in controlling intracellular pathways in response to external cell signaling (Gautreau et al., 1999).

Accumulating evidence has shown that the AKT-mediated Tuberous Sclerosis Complex (TSC complex) phosphorylation is a major mechanism in triggering the activity of the GTPase Rheb (Ras homolog enriched in brain), an essential activator of mTORC1 at lysosomes. We demonstrated recently that Ezrin is a key regulator of lysosomal biogenesis and functions in RPE/retina crosstalk by modulating TFEB nuclear translocation (Naso et al., 2020). Moreover, Ezrin overexpression leads to altered autophagy and an impairment of POS maturation and degradation in RPE cells (Naso et al., 2020). Thus, it is intriguing that Ezrin has been recently observed to be associated with lysosomes

(Poupon, Stewart, Gray, Piper, & Luzio, 2003). Furthermore, cancer cell proliferation and invasion through an activated Akt/mTORC1 pathway was linked with activation of Ezrin (Krishnan et al., 2006). In contrast, depletion of Ezrin was found to be associated with the repression of the mTORC1 pathway (Wan, Mendoza, Khanna, & Helman, 2005). Together, these data led us to hypothesize that Ezrin-mediated EGFR endosomal sorting and trafficking could play a central role in mTORC1 activation on lysosomes.

Here, we identify a previously undocumented function for Ezrin as a platform that is essential for the endosomal signaling network involving EGFR and AKT pathways, which provides an important insight into the spatial inactivation of the TSC complex on endosomal compartments. We show that inactivation of Ezrin is crucial to neutralize EGF-stimulated EGFR endosomal sorting and signaling from the plasma membrane with a reduction of AKT-mediated phosphorylation of TSC complex, which in turn translocates and inhibits mTORC1 on lysosomes. These results reveal an essential layer of mTORC1 regulation by Ezrin and EGFR signaling and uncover part of the paradigm of signaling from endosomes to lysosomes to coordinate the lysosomal function in the retina and other tissues. Consistent with the role of the Ezrin/EGFR/TSC complex axis in lysosomal biogenesis and function, alteration of this molecular network alters autophagy in vivo in Medaka fish, resulting in retinal degeneration. Derangement of this control mechanism may underpin human eye disorders and may be relevant as a therapeutic target to restore normal vision.

RESULTS

Ezrin regulates lysosomal biogenesis.

Activated Ezrin represses the autophagy pathway in the RPE (Naso et al., 2020), but the mechanism remains undefined. To gain insights into this, we used integrated comparative analysis by unbiased

RNA-seq and high□resolution mass spectrometry□based proteomic studies on Ezrin$^{-/-}$ mouse embryonic fibroblasts (MEFs) (EZR^{KO}) (Ognibene et al., 2011). The comparison of the transcriptomics and proteomics identified 572 commonly regulated genes: 317 and 213 genes are induced and inhibited in both datasets, respectively (Figure supplement 1A). Gene Ontology (GO) and Functional Annotation Clustering analyses were performed on these 530 commonly differentially expressed genes (DEGs), restricting the output Cellular Compartments (CC) terms (Tables supplement 1-3). We found an enriched overlap of these genes in cell compartments, including cell membrane and lysosome (Figure 1A, Figure supplement 1A and supplement 1B and Tables supplement 1-3). Consistent with this, immunofluorescence analysis revealed that the EZR^{KO} displayed an increased number of lysosomes, as assessed by quantification of lysotracker-fluorescent staining and Lamp1-LC3 colocalization (Figure 1B-F). Compared with WT MEFs, lysosomal Cathepsin B (CTSB) activity of EZR^{KO} MEFs was significantly increased (Figure 1G). Furthermore, western blot analysis also revealed that EZR^{KO} increased the expression of lysosomal markers (LAMP1, CTSD and LC3) as well as reducing the levels of the autophagy substrate p62 and NBR1 (Figure 1H). To further investigate whether this autophagic induction was Ezrin dependent, we inserted a frameshift deletion of 13 nt in the coding region (exon 2) of the *EZRIN* gene in HeLa cells via CRISPR/Cas9-mediated genome editing (EZR$^{-/-}$) (Figure supplement 1D). Concordantly, we found that EZR$^{-/-}$ cells have a significantly increased number of lysosomes and increased lysosomal activity (Figure supplement 1E-G), indicative of augmented lysosomal biogenesis and function. Consistent with this, western blot analysis showed that autophagic flux and lysosomal markers were also increased in EZR$^{-/-}$ compared to control (Figure supplement 1H and I). Notably, we found TFEB nuclear localization as a consequence of Ezrin depletion (Figure supplement 1J), in line with previous results (Naso et al., 2020). Taken together, these results reveal the crucial roles of Ezrin in lysosomal biogenesis and function. These results are consistent with our

previous report showing that the autophagy pathway is blocked by Ezrin overexpression *in vivo* (Naso et al., 2020).

Ezrin interacts with EGFR and regulates its activation.

Previous studies have implicated Ezrin in coordinating signaling complexes on membranes in cancer, raising the question of whether the Ezrin-mediated control of autophagy may be attributed to an alteration of signaling pathways. To identify potential signaling pathways affected by Ezrin modulation, we performed an enrichment analysis of the 530 differentially expressed genes in EZR^{KO}, using stable isotope labeling by amino acids in cell culture (SILAC) phosphoproteomics, kinase perturbations from GEO database, and the Proteomics drug atlas. Interestingly, SILAC phosphoproteomics data highlighted a significant overlap with phosphorylation changes in HeLa cells upon EGF treatment (Figure 2A and Table supplement 4). Accordingly, kinase perturbation revealed a significant overlap with downregulated genes upon EGFR drug activation (Figure supplement 2A and Table supplement 4), whereas Proteomics drug atlas revealed a significant enrichment in cells upon AZ628 (a Raf Inhibitor) or MEK162 (a MEK inhibitor) (Figure supplement 2B and Table supplement 4) (B. Liu, Chen, Johns, & Neufeld, 2006; Mitchell et al., 2023; Olsen et al., 2006; Ong et al., 2002; Warde-Farley et al., 2010) (All resources are available https://maayanlab.cloud/enrichr-kg/downloads). Thus, we hypothesized that the EGFR needs to be selectively recognized by EZRIN to be subjected to EZRIN-mediated endosomal trafficking and signaling. Consistent with this, gene network based on physical interaction reveals EGFR as a possible direct EZRIN protein partner (Figure 2B and Table supplement 5). Moreover, EGFR resulted strongly upregulated in our omics dataset (Figure 2C) and co-immunoprecipitation (CoIP) experiments revealed a complex composed of EZRIN and EGFR (Figure 2D), consistent with human biomedical interaction repositories (Oughtred et al., 2021; Petschnigg et al., 2014; Salokas et al., 2022). To further detail this possible interaction, we assessed all possible

188 pairwise interactions between the known domains of Ezrin UID:P15311 and EGFR (UID:P00533) by
189 mining 3did (10.1093/nar/gkt887) and PPIDomainMiner (10.1371/journal.pcbi.1008844) (Figure
190 supplement 2C). Interestingly, the EZRIN-EGFR interaction appears to occur between the FERM
191 central domain (PF00373) of Ezrin with the PK domain (PF07714) of EGFR, in line with previous
192 structural studies by X-ray diffraction in which was patterned a direct interaction of the FERM domain
193 with kinase domain of focal adhesion kinase (FAK) (Lietha et al., 2007). Phosphorylated Ezrin
194 (Thr567) localizes at curved cytoplasmic membranes and has been implicated as a membrane-
195 cytoskeleton scaffolding protein rather than a membrane shaper (Tsai et al., 2018). We therefore tested
196 whether phosphorylation at Thr567 of Ezrin was involved in interacting with EGFR in a complex at
197 cytoplasmic membrane. As hypothesized, phosphomimic active-EZR^{T567D}, but not phospho-mutant
198 inactive-EZR^{T567A} protein (Naso et al., 2020), when expressed in EZR$^{-/-}$ cells, highly co-
199 immunoprecipitated with EGFR (Figure 2E). These data support that active EZRIN protein interacts
200 with EGFR. Co-immunostaining analysis confirmed that EZRIN is localized at the plasma membrane
201 with EGFR (Figure 2F). Moreover, a fraction of the EZRIN signal colocalizes with EGFR, within same
202 intracellular compartments (Figure 2F), supporting the presence of an EZRIN/EGFR complex, in which
203 EZRIN acts as a scaffold protein for EGFR. Thus, we postulated that EZRIN participates in EGFR
204 trafficking and signaling. To test this hypothesis, we examined the expression levels and subcellular
205 distribution of EGFR under normal and EZRIN-depleted conditions by immunofluorescence staining
206 and Western blot (Figure 2G-I). Interestingly, the genetic depletion of EZRIN strongly induced a
207 statistically significant localization of EGFR at the plasma membrane and dramatically reduced its
208 presence within intracellular compartments (Figure 2G and H). Considering that the specific EGFR
209 signals can arise from intracellular compartments, such as the endosomal compartment (Burke,
210 Schooler, & Wiley, 2001), we examined whether EZRIN depletion would impair EGFR signaling.
211 Consistent with proteomic results, we found that the levels of total EGFR are increased in EZR$^{-/-}$

compared to control cells (Figure 2I). However, western blot analysis demonstrated that the absence of EZRIN induced a reduction in EGFR signaling. Notably, the level of HER3 and active pY845 EGFR were almost abolished following EZRIN depletion, in line with previous results where disruption of wild-type EGFR signaling induced reduction of HER3 (B. Liu, Chen, Chen, Saber, & Haisma, 2020). Interestingly, lack of EZRIN also reduced the EGFR-stimulated phosphorylation of p38 MAPK at Threonine 180 (T180) and Tyrosine 182 (Y182). However, we noticed an increased phosphorylation at T222 of its substrate, MK2 (Figure 2I). The latter result could be due to an activation of the ERK pathway that might attenuate EZRIN/EGRF-dependent reduction of p38 MAPK signaling. Indeed, ERK2 binds and phosphorylates MK2 (Sok et al., 2020). Future studies will be needed to investigate ERK1/2 signaling is part of the EZRIN/EGFR-mediated signaling network. Taken together, these data suggest a model by which the EZRIN interaction with EGFR contributes to EGFR trafficking and signaling.

Ezrin regulates endocytic EGFR sorting and signaling.

Activation of EGFR leads to its internalization and trafficking to early endosomes, which sustains specific EGFR signaling and recycling (Burke et al., 2001). We asked if the increased EGFR protein level at cell membrane and the reduction of EGFR signaling in $EZR^{-/-}$ cells could be due to an alteration in EGFR dimerization and packaging into endosomal vesicles. To test this hypothesis, the cellular internalization and trafficking of EGFR basis was investigated by immunofluorescence and live-imaging studies. We found that the lack of Ezrin statistically reduced dimerization of EGFR upon EGF stimulation (Figure 3A and B). These results were confirmed by immunofluorescence analyses; indeed, compared to control cells, Ezrin-depleted cells showed higher levels of EGFR on the cell surface, which was mirrored by reduced EGFR abundance at endosomal compartments, as assessed by a reduction in the overlap between EGFR and EEA1 signals (Figure 3C and D) and increased EGFR

protein levels on purified membranes (Figure 3E-F upper panels). Consistently, EGFR endosomal localization was present on purified endosomes from control but not from $EZR^{-/-}$ cells (Figure 3E-F lower panels). The reduced internalization of EGFR to endosomes was not accompanied by a suppression of endocytosis, as indicated by the slight and significant increase in the number of EEA1-positive early endosomes and endotracker-positive structures in $EZR^{-/-}$ compared to WT cells (Figure 3G and H). These results support that EGFR accumulation at the plasma membrane was not a result of an endocytosis defect. To better define whether the lack of EZRIN alters EGFR internalization and trafficking in $EZR^{-/-}$ cells upon EGF stimulation, we performed Total Internal Reflection Fluorescence (TIRF) time-lapse imaging at high spatiotemporal resolution. Both $EZR^{-/-}$ and control cells, transfected with an EGFR-GFP vector, were imaged every 0.5□s for 5 min upon EGF treatment. Notably, the EGF-induced EGFR endosomal internalization was dramatically abolished in $EZR^{-/-}$ compared to control cells (Figure 4A-C, Figure 5A and Video 1-4). Consistent with a defective EGFR integration in the early endosome, EGFR was localized at the plasma membrane in $EZR^{-/-}$ cells, despite EGF stimulation (Figure 4A-C, Figure 5A and Video1-4). These results suggest that EZRIN play an important role for the dimerization, integration, and trafficking of EGFR in the endosomes. To strengthen these findings, we performed ultrastructural analysis using immunoelectron microscopy (IEM) that further revealed the reduced number of EGFR-positive endosomal compartments and the increased presence of EGFR at the plasma membrane in EGF-stimulated $EZR^{-/-}$ compared with EGF-stimulated control cells (Figure 5B). Consistent with this, pY845 EGFR, pY1068 EGFR, pT202/Y204 p44/42 MAPK, and pT180/pY182 p38 MAPK were reduced upon EGF stimulation in $EZR^{-/-}$ cells (Figure 5C). Moreover, the increased EGFR internalization from membranes to endosomes by EGF stimulation was significantly inhibited in $EZR^{-/-}$ cells compared to WT (Figure 5D). As expected, we found that the endosomal EGFR internalization was further repressed in MEF-EZR^{KO} (Figure supplement 2D-H) and in HeLa cells upon *NSC668394* treatment (Figure supplement 3A-B), a specific

Ezrin inhibitor (Naso et al., 2020). Taken together, these data strongly support a primary role of EZRIN in mediating the internalization and trafficking of EGFR from plasma membrane to endosomes.

The endosomal Ezrin-EGFR complex targets TSC complex protein

We next sought to identify the molecular networks by which Ezrin/EGFR axis controls lysosomal biogenesis and function. Interestingly, EGFR stimulates several downstream effectors, including PI3K/AKT signaling in response to multiple stimuli (Wee & Wang, 2017). This led us to investigate the role of Ezrin/EGFR axis in the control of AKT signaling. AKT binds, phosphorylates, and inhibits hamartin (TSC1) and tuberin (TSC2) complex. TSC complex is essential to turn off the activity of Rheb, a crucial activator of mTORC1 at lysosomal surface (Dibble & Cantley, 2015). This raised the possibility of Ezrin-mediated activation of EGFR signaling would be required for AKT activation and thus stimulation of the mTORC1 pathway via TSC complex repression. To test this hypothesis, we analyzed the interaction between endogenous Ezrin/EGFR with AKT and TSC1 to define an endosomal signaling platform. In agreement with previously presented data (Haddad et al., 2002), TSC1and AKT co-immunoprecipitated with EZRIN (Figure 6A upper panel). We also noticed that Ezrin was able to interact with TSC2 (Figure 6A upper panel). The molecular basis of these interactions was investigated by *in silico* domain-domain interaction analyses. Accordingly, EZRIN (UID:P15311) was found as a scaffold protein interacting through its FERM central domain with the PK domain of EGFR, as detailed above (Figure supplement 2C), and binding TSC1. Although Alphafold3 modeling of the EZRIN/TSC1 dimer did not provide high-confidence results, suggesting that the TSC1 (PF04388) could interact with both FERM N-terminal (PF09380) and C-terminal (PF09379) domains of EZRIN (Figure supplement 3C-H). Concordantly, PPIDomainMiner identifies the FERM-N/C-hamartin as moderately confident (silver class), further supporting the possibility of EGFR/EZRIN/TSC1 interactions. Consistently, immunoprecipitation of EGFR was able to pull down

both TSC1 and AKT (Figure 6A lower panel), suggesting that EGFR, AKT, TSC1 and EZRIN are present in a complex. The latter results led us to investigate whether EGFR could interact with AKT and TSC1 indirectly through EZRIN. Co-immunoprecipitation experiments confirmed this possibility, given that *EZRIN* depletion abolished the interactions of EGFR with TSC1 and AKT, thereby pointing out the role of Ezrin as a scaffold protein for the formation and activation of the EGFR/AKT/TSC1 signaling (Figure 6A). In agreement with this hypothesis, the lack of Ezrin reduced pS473 AKT activation and in turn suppressed AKT-mediated phosphorylation of pS939 TSC2 (Figure 6B). As expected, the inactivation of AKT promoted activation of TSC1 and TSC2, which localized on the lysosomes in $EZR^{-/-}$ cells (Figure 6D and E). Consistently, translocation of the TSC complex on the lysosomes led to inhibition of mTORC1 pathway, as demonstrated by reduction of pT389 P70 S6 Kinase and pS65 4E-BP1 levels (Figure 6B). In agreement, the insulin administration was not able to restore mTORC1 signals (Figure 6C) and lysosomal localization of TSC complex in $EZR^{-/-}$ cells (Figure supplement 3J), in line with the hypothesis that Ezrin acts as a scaffold protein for AKT/TSC complex. Thus, we ensured that these findings were also confirmed when EZRIN was pharmacologically inhibited on HeLa (Figure supplement 4A) and ARPE-19 cells (Figure supplement 4B and C). Concordantly, these results were mirrored in MEF EZR^{KO} cells that yield a similar pattern (Figure supplement 4D and E). To strengthen the molecular mechanism by which EGFR/EZRIN controls mTORC1 pathway via TSC complex, we investigated the effects of EZRIN inhibition on MEF $TSC2^{KO}$ cells and found that depletion of TSC2 rescue TORC1 signaling when Ezrin was pharmacologically inhibited (Figure supplement 4F). Together, these results establish an Ezrin-dependent molecular machinery coordinating EGFR sorting and signaling at the endosome to a well-regulated signals transfer to lysosomes via AKT/TSC complex axis. Consistent with this idea, phosphorylation of pS473 AKT was significantly abolished in response to EGF treatment in $EZR^{-/-}$ compared to control cells (Figure 6F). Accordingly, using confocal Airyscan high-resolution

308 microscopy, we found that the majority of the TSC complex was present in early endosomes of HeLa
309 WT cells upon EGF treatment, as shown by co-localization with the endosomal marker EEA1 (Figure
310 6G and H). Notably, the endosomal TSC complex localization was abolished in EGF-treated $EZR^{-/-}$
311 cells (Figure 6G and H), which indicates that EGFR-mediated repression of TSC complex by AKT
312 activation could occur in a stable endosomal complex dependent on Ezrin. Consistently, the ectopic
313 expression of a constitutively active EZR^{T567D} protein, but not a constitutively inactive Ezr^{T567A} protein,
314 rescued EGFR sorting and signaling activation at the endosome in $EZR^{-/-}$ cells upon EGF treatment
315 (Figure supplement 5A). Additionally, EZR^{T567D}, but not EZR^{T567A}, rescued the physiological
316 localization of TSC complex on the cytoplasm in $EZR^{-/-}$ cells (Figure supplement 5B). Moreover, full
317 translocation of TSC complex on endosomes was restored in $EZR^{-/-}$ cells expressing EZR^{T567D} protein
318 after EGF treatment, as shown by co-localization between TSC1 and EEA1 proteins (Figure
319 supplement 5B).
320
321 **Aberrant EGFR signaling induces retinal degeneration in $EZR^{-/-}$ medaka fish.**
322 To further investigate the role of EZRIN/EGFR axis, which is conserved among vertebrates, in daily
323 modulation of lysosomal biogenesis and function in retinal cells, we carried out *in vivo* experiments.
324 Accordingly, we found that the EGFR expression pattern in the rodents' retina diminished in response
325 to light and increased after light off (Figure supplement 6A and B), coinciding with Ezrin expression
326 and diurnal lysosomal biogenesis in the RPE/retina (Naso et al., 2020). Consistently, we found an
327 inhibition of TSC2 and an increase of AKT/mTORC1 pathway in the mice retina in response to dark
328 condition, when active Ezrin (Naso et al., 2020) and EGFR are highly expressed (Figure supplement
329 6C). Moreover, we found that TSC2 was dephosphorylated in response to light in the retina, when
330 inactive Ezrin (Naso et al., 2020) and EGFR are weakly expressed (Figure supplement 6C) as a
331 consequence of a decrease of the AKT/mTORC1 signaling, which suggests that activation of Ezrin

underlies the requirement endosomal EGFR signaling to assemble the EGFR/AKT/TSC complex and represses lysosomal biogenesis. This data supported that EGFR signaling in retinal cells could be regulated by Ezrin for finely control lysosomal biogenesis and function in mTORC1-dependent manner. Thus, we used the highly effective CRISPR-Cas9 mediated mutagenesis to create stable Ezrin mutant lines in Medaka fish (*Oryzias latipes,* Ol) as *in vivo* model system. Targeting two sgRNAs (sgRNA1 and sgRNA2) in the exon 1 of *Ezrin* gene, we generated a 386 bp deletion and established founder lines for this deletion. This mutation eliminates the first 129 amino acids containing ATG (olEzrin$^{\Delta 386}$), generating a severely truncated Ezrin protein (Figure 7A), which was not detectable by western blot analyses (Figure 7B). This indicated that the Δ386 Ezrin allele is likely functionally null, and mutants will hereafter be called Ezrin$^{-/-}$ medaka line. Larval homozygous Ezrin$^{-/-}$ medaka line appeared almost visually indistinguishable from wild-type siblings, and the Δ386 allele was inherited in Mendelian ratios (Figure 7C). Interestingly, the Ezrin$^{-/-}$ medaka larvae recapitulated in part a previously reported phenotype characterized in postnatal ezrin knockout mice (Bonilha, Rayborn, Saotome, McClatchey, & Hollyfield, 2006). Consistent with our *in vitro* data, we observed increased levels of the EGFR protein accompanied by a significant reduction of active pY845 EGFR. This was associated by a significant reduction of the phosphorylation of pS473 AKT in Ezrin$^{-/-}$ Medaka line compared to control larvae (Figure 7D). Consistently, we observed reduced AKT-mediated phosphorylation of pT1462 of TSC2, decreased mTORC1 signaling as shown by reduction of p4EBP1 (S65) and an increased autophagy, as demonstrated by higher levels of LC3-II and Lamp1 (Figure 7D and E). Notably, endosomal internalization of EGFR was significantly repressed in the RPE of Ezrin$^{-/-}$ medaka line. Consistent with defective EGFR internalization and trafficking, whole mount immunofluorescence analysis showed that EGFR accumulated at plasma membrane of RPE of Ezrin$^{-/-}$ medaka line compared with control fish (Figure 7F). Considering the role of endosomal sorting and signaling in the health of retinal cells (Toops, Tan, & Lakkaraju, 2014), we addressed the consequences of aberrant EGFR

signaling pathway in retina of Ezrin$^{-/-}$ medaka line. Notably, defective endosomal EGFR signaling was sufficient to induce deleterious consequences for the health of photoreceptor cells, which showed reduction in photoreceptor outer segments compared with native rods (Figure 7G), similarly to the pathogenesis of macular degeneration (Borrelli et al., 2020; Kaur & Lakkaraju, 2018). Notably, depletion of *olEzrin* was also associated with a significant increase in the number of TUNEL-positive cells in the retina from Ezrin$^{-/-}$ medaka compared to control (Figure 7H). Altogether, these data support the dynamic regulation of EGFR signaling at endosomal compartments in response to Ezrin activation, which assembles and activates an EGFR/AKT/TSC complex signalosome at endosomes to finely regulate the lysosomal signaling by mTORC1 pathway, required for the correct autophagy and retinal cell health (Figure 8).

DISCUSSION

Canonical EGFR signaling begins at the plasma membrane with the engagement of the EGF ligand (Tanaka et al., 2018). Emerging studies have indicated that sorting of the EGF-EGFR complex to endosomal vesicles requires spatiotemporally defined encounters with distinct cytoskeleton platforms resulting in internalization, activation, maintenance or termination of EGFR signaling (Ceresa, 2012; Wang, Pennock, Chen, & Wang, 2002). Consistent with this notion, it is now increasingly recognized that many molecules participating in signal transduction are central sorting hubs that coordinate signaling from and to different intracellular compartments, including early endosomes, late endosomes, phagosomes, and lysosomes (Sorkin & von Zastrow, 2009). However, molecular networks determining selective signal transduction from endosomes to lysosomes are not well defined. In this study, we demonstrated that EZRIN is a cytoskeleton scaffold protein aligned along internal membranes, and that this localization is essential for endosomal EGFR signal transduction to the TSC complex. Endosomal

EGFR sorting and activation occurs mainly due to binding with EZRIN that facilitates dimerization and activation of the EGF-EGFR receptor complex, resulting in their recruitment to endosomes, followed by AKT activation that targets and inhibits the TSC complex. Indeed, time-lapse confocal imaging revealed that EGFR fails to be recruited to endosomal compartments upon EGF stimulation in the absence of Ezrin or in the presence of its inactive form ($EZRIN^{T567A}$). The loss of Ezrin function compromises EGFR-mediated AKT activation, which in turn reduces TSC complex inhibition resulting in TSC complex translocation to lysosomes where it constrains mTORC1 activity. Consistent with this, not only does loss of Ezrin impact on lysosomal TSC complex translocation, but we also documented that dephosphorylation of Ezrin in its inactive form is required for EGFR inactivation and TSC1 and TSC2 release from an EGFR/EZRIN complex, possibly to support the lysosomal biogenesis and function. Indeed, autophagy appears to be highly sensitive to pharmacological Ezrin inhibition via the EGFR/AKT axis. Moreover, overexpression of $EZRIN^{T567A}$, but not $EZRIN^{T567D}$, fails to restore EGFR endosomal signaling and lysosomal function in Ezrin-defective cells, indicating that phosphorylation of Ezrin is indispensable for this activity. Supporting this possibility, loss of βA3/A1-crystallin affects PITPβ/PLC signaling axis associated with an age-related loss of PLC-mediated Ezrin phosphorylation and subsequent compromised RPE cell polarity and EGFR signaling. Notably, the lysosome-mediated POS clearance was disrupted in the Cryba1 cKO RPE (Shang et al., 2021). Beyond this, our findings also showed an interaction of EGFR with the TSC complex and their co-localization with endosomes, opening to future work on mechanisms of how endosomal system connects extracellular signals with lysosomes under different physiological and pathological conditions.

Upregulation of Ezrin has been shown to induce an age-related macular degeneration-like phenotype in miR-$211^{-/-}$ mice (Naso et al., 2020), where light-mediated cell clearance is completely abolished. We can speculate that recruitment of EGFR on endosomal compartments by Ezrin orchestrates a local signal between endosomes and lysosomes to drive tight control on the lysosomal cargo demands,

403 although future studies are needed in this regard. Interestingly, inhibition of EGFR activity, by
404 silencing Rubicon (RUBCN), switches lysosomal cargo degradation from POS associated to LC3-
405 associated phagocytosis to autophagy process in the RPE cells (Muniz-Feliciano, Doggett, Zhou, &
406 Ferguson, 2017). However, the molecular mechanisms are completely unknown. Therefore, Ezrin may
407 represent a nodal point in endosomal compartments where EGFR signaling and AKT converge and
408 integrate to directly control the TSC complex/mTORC1 pathway and lysosomal cargo demands and
409 degradation. Notably, mutations affecting TSC1 and TSC2 alter lysosomal function with retinal
410 manifestations in 40–50% of individuals (Rosset, Netto, & Ashton-Prolla, 2017). This phenotype is
411 also showed in RPE-specific deletion of TSC1 profoundly leading to an age-related impairment in
412 lysosomal function associated with RPE degeneration *in vivo* (Huang et al., 2019).
413 The findings of the cellular mechanisms governing endosomal EGFR sorting and signaling might be of
414 therapeutic relevance. Indeed, alteration of endosomal biogenesis and signaling have been shown to
415 participate in the age-related, progressive neurodegeneration such as in age-related macular
416 degeneration and Alzheimer's disease (REF Kaur et al). Thus, the identification of the mechanisms that
417 control Ezrin/EGFR/mTORC1 molecular network might be exploited for the treatment of diseases in
418 which defective endo-lysosomes play a part.
419

420 **MATERIALS AND METHODS**

421 **3' mRNA sequencing library preparation**

422 The transcriptional response of four biological replicates for both MEF^{WT} and MEF^{Ezr} KO cell lines
423 was analyzed using QuantSeq 3' mRNA sequencing. RNA extraction, quality control and preparation
424 of RNA-seq libraries and sequencing on an NovaSeq6000 platform were carried out in collaboration
425 with the Next Generation Sequencing (NGS) Facility at TIGEM following their standard procedures

(Carotenuto et al., 2022). An average yield of ~4.5 Mb was obtained per sample.

Computational analysis of deep sequencing data

Data analysis was performed using the pipeline already established at the Bioinformatics and Statistics Core Facility at TIGEM (Pinelli et al., 2016). Briefly, the reads were trimmed to remove adapter sequences and low-quality ends and reads mapping to contaminating sequences (e.g. ribosomal RNA, phIX control) were filtered-out. Alignment was performed with STAR 2.6.0a3 (Dobin et al., 2013) on mm10 reference assembly obtained from cellRanger website4 (Ensembl assembly release 93). The expression levels of genes were determined with htseq-count 0.9.15 using mm10 Ensembl assembly (release 93) downloaded from the cellRanger website4. We filtered out all genes having < 1 cpm in less than n_min samples and Perc MM reads > 20% simultaneously. Differential expression analysis was performed using edgeR6 (S. Liu et al., 2021).

Mass Spectrometry

Protein extraction and preparation of MS samples were carried out in accordance with standard procedures currently utilized in the Mass Spectrometry Facility at TIGEM. About 30 mg of cell lysate was used. Peptides were purified using the iST Kit (Preomics) following the company instructions. Peptide separation and LC MS/MS analysis was carried out accordingly to standard procedures as detailed in (Di Malta et al., 2023)

Data analysis of mass spectrometry

At least three independent biological replicates were performed for all experiments. For mass spectrometry, all acquired raw files were processed using MaxQuant (1.6.2.10) and the implemented Andromeda search engine. For protein assignment, spectra were correlated with the UniProt Homo

Sapiens including a list of common contaminants. Searches were performed with tryptic specifications and default settings for mass tolerances for MS and MS/MS spectra. Carbamidomethyl at cysteine residues was set as a fixed modification, while oxidations at methionine and acetylation at the N-terminus were defined as variable modifications. The minimal peptide length was set to seven amino acids, and the false discovery rate for proteins and peptide-spectrum matches to 1%. The match-between-run feature with a time window of 0.7 min was used. For further analysis, the Perseus software was used and first filtered for contaminants and reverse entries as well as proteins that were only identified by a modified peptide. For full proteomes and IP-interactomes, the LFQ Ratios were logarithmized, grouped and filtered for min. valid number (min. 3 in at least one group). Missing values were replaced by random numbers that are drawn from a normal distribution. Finally, the intensities were normalized by subtracting the median intensity of each sample. Significantly regulated proteins between conditions were determined by student t-test using FDR < 0.05 as threshold.

Functional analysis on transcriptomics and proteomics data

The threshold for the statistical significance of gene expression was FDR < 0.05. The threshold for the statistical significance of the proteomics analysis was -log10 > 1,3 and -Log2 > =1. GOEA and KEGG Pathway were performed on induced and inhibited genes, separately, both in the transcriptome and in the proteome experiments using the DAVID Bioinformatic tool (Huang da, Sherman, & Lempicki, 2009a, 2009b) restricting the output to Biological Process (BP), Cellular Compartments (CC) terms. The threshold for statistical significance of GOEA was FDR <0.1 and the Enrichment Score ≥ 1.5, while for the KEGG Pathway analyses it was FDR < 0.1. The comparison of the transcriptomics and proteomics identified 572 commonly regulated genes: 317 and 213 genes were induced and inhibited in both datasets, respectively.

Data visualization

Heatmap and Venn diagram were generated using custom annotation scripts.

Accession code

The transcriptomics data have been deposited in the NCBI Gene Expression Omnibus (GEO) (Edgar, Domrachev, & Lash, 2002) and are accessible through GEO Series accession number GSE195983**.** The title of the dataset is: "Transcriptome profile of EZR_KO cells"**.** For this dataset, a secure token has been created to allow a review of the record: private token. The proteome data was deposited in PRIDE repository and are available via ProteomeXchange with identifier PXD045157.

Alpha fold

All protein pairs were modeled using AlphaFold3 (Abramson et al., 2024) through ChimeraX, using the alphafold dimers command to generate a JSON af3 query. The FASTA input for the command was downloaded from UniProt (https://www.uniprot.org). AlphaFold3 was run with default settings and random seed. The resulting structures were evaluated by analyzing the predicted Local Distance Difference Test (pLDDT) scores, Predicted Aligned Error (PAE) matrices, and protein interfaces with the alphafold interfaces command in ChimeraX. Simple bash/R scripts were used to mine associations between Pfam domains in the UniProt entries across various databases (PPIDM, 3DID, DOMINE). The domain interaction network was built in R (R Core Team (2024). _R: A Language and Environment for Statistical Computing_. R Foundation for Statistical Computing, Vienna, Austria. <https://www.R-project.org/>.) with tidyverse (doi.org/10.21105/joss.01686) and igraph (10.5281/zenodo.7682609) and visualized using ggraph (https://CRAN.R-project.org/package=ggraph). All structural visualization/analyses were run with ChimeraX (Pettersen et al., 2021).

Western blot analysis

After transfection and/or treatments, cells were collected to extract total protein, while mouse eyes were enucleated, and the retina was separated from the RPE. Both mice and cell samples were lysed using RIPA buffer (150 mM sodium chloride, 1% Triton X-100, 0.5% sodium deoxycholate, 0.1% sodium dodecyl sulfate, 50 mM Tris, pH 8.0) with an inhibitor cocktail (Thermo Fisher Scientific, 78420). The protein concentration was determined by Bradford analysis and quantified using a Thermo Fisher Helios γ spectrophotometer. Proteins were fractionated by sodium dodecyl sulfate-polyacrylamide gel electrophoresis (SDS-PAGE) and transferred to PVDF membranes (EMD Millipore, IPVH00010), then blocked in Tween 0.1% Tris-buffered saline containing 5% bovine serum albumin (Tocris 5217) for at least 1h at room temperature and subsequently incubated overnight at 4°C with primary antibodies. For Western blot analysis, the following antibodies were used: mouse anti-NBR1 (1:1000, Abnova MO1), rabbit anti-LAMP1 (1:500, Sigma L1418), mouse anti-Ezrin (1:1000, Novex 357300), mouse anti-SQSTM1/P62 (1:1000, Abcam ab56416), rabbit anti-Cathepsin D (1:1000, Cell Signaling 2284), rabbit anti-LC3 (1:1000, Novus NB100-2220), mouse anti-GAPDH (1:1000, Santa Cruz SC-32233), rabbit anti-HER2/ErbB2 (1:1000, Cell Signaling 2165), rabbit anti-HER3/ErbB3 (1:1000, Cell Signaling 12708), rabbit anti-phospho-EGF receptor (Tyr845) (1:1000, Cell Signaling 6963), rabbit anti-EGF receptor (1:1000, Cell Signaling 4267), rabbit anti-MAPKAPK-2 (1:1000, Cell Signaling 3042), rabbit anti-phospho-MAPKAPK-2 (Thr222) (1:1000, Cell Signaling 3316), rabbit anti-p38 MAPK (1:1000, Cell Signaling 8690), rabbit anti-phospho-p38 MAPK (Thr180/Tyr182) (1:1000, Cell Signaling 4511), rabbit anti-ZO1 (1:1000, Abcam ab216880), mouse anti-EEA1 (1:1000, BD 610457), rabbit anti-Tuberin/TSC2 (1:1000, Cell Signaling 4308), rabbit anti-phospho-Tuberin/TSC2 (Ser939) (1:1000, Cell Signaling 3615), rabbit anti-phospho-Tuberin/TSC2 (Thr1462) (1:1000, Cell Signaling 3617), rabbit anti-p70 S6 Kinase (1:1000, Cell Signaling 9202), mouse anti-phospho-p70 S6 Kinase (Thr389) (1:1000, Cell Signaling 9206), rabbit anti-Akt (1:1000, Cell Signaling 9272), rabbit anti-phospho-Akt (Ser473) (1:1000, Cell Signaling 4060), rabbit anti-4E-

BP1 (1:1000, Cell Signaling 9644), rabbit anti-phospho-4E-BP1 (Ser65) (1:1000, Cell Signaling 9456), rabbit anti-phospho-4E-BP1 (Thr37/46) (1:1000, Cell Signaling 2855), rabbit anti-Hamartin/TSC1 (1:1000, Cell Signaling 6935), mouse anti-EGFR (1:500, Santa Cruz sc-120), mouse anti-p-EGFR (1:500, Santa Cruz sc-57542). After washing 3 times with Tween 0.1% Tris-buffered saline (TBS-T), the membranes were incubated for 1 h at room temperature with the following secondary antibodies: goat anti-rabbit IgG antibody, HPR conjugate, and goat anti-mouse IgG antibody HPR conjugate (1:10,000 EMD Millipore, 12-348; 12-349). Western blot detection was done with ChemiDoc XRS+ System-Bio-Rad and quantified using ImageJ software.

Immunofluorescence

Mouse eyes were fixed overnight in 4% paraformaldehyde in PBS at 4°C and then cryopreserved by treatment first with 5% and then with 30% sucrose in phosphate-buffered saline and embedded in OCT. Twenty-micrometer cryosections were collected on slides (Superfrost Plus; Fisher Scientific, Pittsburgh, PA). Cells were fixed with 4% paraformaldehyde (Chem Cruz sc-281692) for 15 min at room temperature followed by washing with 1% PBS. After fixation, the cells were permeated with blocking buffer (0.5% BSA, 0.005% saponin, 0.02% NaN_3) for 1 h at room temperature. Medaka fish at stage 40 were subjected to anesthesia and then fixed by incubation in 4% PFA for 4 h at room temperature (RT). Samples were rinsed three times with PTW 1X (1X PBS, 0.1% Tween, pH 7.3) and then incubated overnight in 15% sucrose/PTW 1X at 4°C, and then again incubated overnight in 30% sucrose/PTW 1X at 4°C and embedded. Sixteen-micrometer cryosection were collected on slides. The following primary antibodies were used: rat anti-LAMP-1 (1:400, Santa Cruz sc-19992), mouse anti-LAMP-1 (1:1000, DSHB H4A3), rabbit anti-LAMP1 (1:100, Abcam ab24170), rabbit anti-LC3B (1:200, Novus NB100-2220), rabbit anti-EGF receptor (1:50, Cell Signaling 4267), mouse anti-EEA1 (1:100, BD 610457), rabbit anti-Tuberin/TSC2 (1:100, Cell Signaling 4308), rabbit anti-

Hamartin/TSC1 (1:1000, Cell Signaling 6935), mouse anti-EGFR (1:50, Santa Cruz sc-120), chicken anti-GFP (1:500, Abcam ab13970), LysoTracker Red (Invitrogen L7528), CellLight Early Endosomes-RFP (Invitrogen C10587). All incubations were performed overnight at 4°C. After washing with 1% PBS, slides were incubated with the following secondary antibodies: Alexa 488 goat anti-rabbit/mouse/Chicken (1:1000, Invitrogen A-11008 rabbit, A-11032 mouse, A-11039), Alexa 594 goat anti-mouse/rat (1:1000, Invitrogen A-11032 mouse, A-11007 rat) and DAPI (1:500, Vector Laboratories H-1200) for 1 h at room temperature; then, the slides were washed with 1% PBS and mounted with PBS/glycerol and imaged with a Zeiss LSM800 microscope. Three dimensional images were imaged with a Zeiss LSM880 confocal microscope equipped with Airyscan super-resolution imaging module, using x63/1.40 NA Plan Apochromat Oil DIC M27 objective lens (Zeiss MicroImaging, Jena, Germany).

Live cell imaging

HeLa cells were transiently transfected with EGFR-GFP and treated as indicated in the Fig.s. Time lapse video were acquired for 5 min. One frame was acquired roughly every 0.5 s with lasers set at 30% power or below. Total Internal Reflection Fluorescence (TIRF) time-lapse imaging was performed with a 60 x Plan Apo oil immersion lens using a Nikon Eclipse Ti Spinning Disk microscope, and images were annotated, and the video was reconstitute using ImageJ software.

Image analysis

Lysotracker and Endotracker quantification. Fluorescent images of the cells were captured at 40 X magnification using a LSM700 Zeiss Confocal Microscopy system, converted to grey-scale and normalized to background staining, using ImageJ. Quantification of lysotracker and endotracker

reactivity was measured as mean values to define fluorescence signal intensity (IntDen/Area) and as the area occupied by fluorescent-labeling in each region of interest.

LC3-LAMP-1, TSC1-LAMP-1 and TSC2-LAMP-1 colocalization. The colocalization of LC3 (green) and LAMP-1 (red) and TSC1/TSC2 (green) and LAMP-1 (red) were evaluated using a LSM700 Zeiss Confocal Microscopy after immunostaining of endogenous proteins. Average values were calculated over 10 images, each containing a mean of 10 cells per image, and collected from at least three independent experiments. Exposure settings were unchanged throughout acquisition. Images were analysed using the JaCoP plugin (Bolte & Cordelieres, 2006) in ImageJ software.

EGFR-positive endosome quantification. Morphometric analysis of the distribution of gold particles (EGFR-labeled) at endosomal structures was performed using iTEM software (Olympus SYS, Germany). In detail, we counted the number of EGFR-positive endosomes on almost 10 26500 x magnification images. In the absence of specific staining, early endosome identification relied on morphological characteristics described in the literature (Vogel et al., 2015).

Cathepsin B assay

Cathepsin B activity was measured by a fluorometric assay kit (AB65300; Abcam, Cambridge, MA, USA) following the manufacturer's instructions. The reaction and fluorescence were read at 400 nm (excitation) and 505 nm (emission) on Promega GloMax discover.

Cross-linking assay

HeLa cells were washed twice with PBS and then cross-linked with DSP solution (Lomant's Reagent, Thermo Fisher 22585) at a final concentration of 1 mM for 30 min at RT. The reaction was stopped by adding stop solution (Tris-HCl 1 M, pH 7.5) at a final concentration of 10 mM for 15 min at RT. Each sample was analyzed by Western blot assay.

Immunoprecipitation assay

Cells were washed three times with ice-cold PBS and then homogenized with ice-cold lysis buffer (20 mM Tris-HCl pH 7.4, 150 mM NaCl, 1 mM EDTA, 0.5% NP40). At least 1 mg of proteins were immunoprecipitated with mouse anti-Ezrin (Novex, 357300) and rabbit anti-EGF receptor (Cell Signaling 4267) in rotation at 4° C overnight. Then, the immunoprecipitates were conjugated with protein G Beads (Dynabeads Protein G, Thermo Fisher Scientific 10004D), eluted in Laemmli buffer, and subjected to immunoblot analyses.

Endosomal and membrane proteins extraction

For endosomal proteins, cultured cells (1×10^6) were collected by low-speed centrifugation and washed with cold PBS. The pellet was resuspended in 500 µl of Buffer solution of Minute Endosome Isolation (Invent, biotechnologies, ED-028). The endosomal proteins extraction was performed in accordance with manufacturer instructions. For membrane proteins extraction, 5×10^6 cells were scraped off from plate surface and resuspended in growth media. After centrifuging the cells, the pellet was washed with Cell Wash Solution and then was resuspended in Permeabilization Buffer, accordingly with manufacturer instructions (Mem-PER Plus Membrane Protein Extraction Kit, Thermo Fisher, 89842).

Cell culture and treatments

ARPE-19, HeLa, and MEF cell lines were obtained from American Type Culture Collection (ATCC). ARPE-19 cells were cultured in Dulbecco's Modified Eagle Medium (DMEM)/F-12, while HeLa and MEF cells were cultured in Dulbecco's Modified Eagle Medium (DMEM) (Gibco) supplemented with 10% (v/v) FBS and 5% penicillin-streptomycin. All cell lines were maintained at 37°C, 5% CO_2 in a humified incubator according to the guidelines provided by the vendors. MEF EZR^{KO} cells were kindly

617 donated by Alessandra Eva of Istituto G. Gaslini, Genova, Italy. To analyze the autophagic flux, cells
618 were treated with 200 nM Bafilomycin A1 (Sigma-Aldrich, B1793) for 3h in an incubator and
619 maintained in starvation for 30 min in HBSS medium (Thermo Fischer Scientific, 14025092)
620 supplemented with 10 mM HEPES (Thermo Fischer Scientific, 156330080). To evaluate EGFR
621 localization in immunoelectron microscopy, HeLa cells were treated with 100 µg/ml cycloheximide
622 (CHX) (Sigma-Aldrich, C4859). Drug treatment was performed for 6 h with 10 µM of *NSC668394* or
623 DMSO as previously reported (Bulut et al., 2012). EGF stimulation was obtained with 10 ng/ml of
624 animal-free recombinant human EGF (Peprotech AF-100-15) for 3h. Insulin stimulation was achieved
625 with 1 µM of Insulin solution human (Sigma I9278) for 30 minutes, after 16 hours of serum starvation.
626 We used a sub-confluent cell culture (i.e. 80% of confluence) for each *in vitro* experiment.

627 **Generation of an EZR$^{-/-}$ HeLa cell line**

628 HeLa (ATCC CCL-2) full knock-out of the *EZRIN* gene was generated using the CRISPr/Cas9 system.
629 The gRNA sequence CAATGTCCGAGTTACCACCA was selected using
630 the http://crispor.tefor.net/crispor.py online tool. HeLa cells were electroporated using the Amaxa
631 system with the nucleofection kit Cat No VCA-1003 from Lonza. Cells were FACS-sorted into 96-well
632 plates to obtain single-cell derived colonies carrying the INDEL mutations. Upon genomic DNA
633 extraction, the genomic sequence containing the targeted region were amplified by PCR reaction with
634 the specific primers: hEZRNup TGCCGTCGCCACACTGAGGA, hEZRNlow
635 TCCTTTGCTTCCATGCCTGG. PCR products were analyzed by DNA Sanger sequencing and the cell
636 clone carrying the homozygous deletion *c.23 DEL AGTTACCACCATG* was selected and expanded.

637

638 **Plasmids and Transfections**

639 Cells were transfected at 80% confluence using Lipofectamine 2000 (Invitrogen, 12566014), following
640 the manufacturer's protocol. The plasmids used were Ezrin^{T567D} and Ezrin^{T567A}-mCherry, modified

from vectors described by Coscoy et al, provided by the S.Coscoy lab (Insitute Curie, Paris) (Coscoy et al., 2002), EGFR-GFP (Addgene, 32751), TFEB-GFP (Addgene, 38119).

Immunoelectron microscopy analysis

HeLa cells were fixed with a mixture of 4% paraformaldehyde (PFA) and 0.05% glutaraldehyde (GA) for 10 min at RT, then washed with 4% PFA once to remove the residual GA and fixed again with 4% PFA for 30 min at RT. Next, the cells were incubated with a blocking/permeabilizing mixture (0.5% BSA, 0.1% saponin, 50-mM NH_4Cl) for 30 min and subsequently with the primary monoclonal antibody anti-GFP, diluted 1:500 in blocking/permeabilizing solution. The following day, the cells were washed and incubated with the secondary antibody, an anti-rabbit Fab fragment coupled to 1.4 nm gold particles (diluted 1:50 in blocking/permeabilizing solution) for 2 h at RT. The cells were then post-fixed as described in Polishchuk and Polishchuk(Polishchuk & Polishchuk, 2019). After dehydration, the specimens were embedded in epoxy resin and polymerized at 60°C for 72 h. Thin 60 nm sections were cut on a Leica EM UC7 microtome. The EM images were acquired from thin sections using a FEI Tecnai-12 electron microscope equipped with a VELETTA CCD digital camera (FEI, Eindhoven, the Netherlands).

Animals and Ethics Approval Statement

All studies on animals were conducted in strict accordance with the institutional guidelines for animal research and approved by the Italian Ministry of Health, Department of Public Health, Animal Health, Nutrition and Food Safety in accordance with the law on animal experimentation (article 31; D.L. 26/2014; protocol number: 0016304-21/07/2020-DGSAF-MDS-P.

RPE and retina dissection

665 To analyze protein expression levels in RPE individually, mouse eyes were dissected to remove optic
666 nerve, cornea, lens, and retina in ice-cold PBS 1X under stereomicroscopy (Leica). The RPE was
667 peeled from the eyecup and transferred to a tube containing 100 µl of RIPA buffer. RPE cells were
668 pelleted by centrifugation at 12,000 x g for 15 min at 4°C.
669
670 **Light/Dark adaptation of mice for tissue isolation**
671 Mice were maintained in dark conditions with a maximum of 0.4 lux from 19:00 pm to 7:00 am. Then,
672 animals were kept in a room with the light phase (450 lux) from 7:00 am to 19:00 pm. For light/dark
673 transition studies, some animals were transferred after 3 h from light conditions to dark conditions and
674 sacrificed. Eyes from dark mice were isolated under dim red light.
675
676 **Medaka stocks**
677 The cab strain of wild-type and Ezrin$^{-/-}$ medaka (*Oryzias latipes*) lines were maintained following
678 standard conditions (i.e., 12h/ 12h dark/light conditions at 27°C). Embryos were staged according to
679 the method proposed by Iwamatsu (Iwamatsu, 2004). All studies on fish were conducted in strict
680 accordance with the Institutional Guidelines for animal research and approved by the Italian Ministry
681 of Health, Department of Public Health, Animal Health, Nutrition and Food Safety in accordance with
682 the law on animal experimentation (D. Lgs.26/2014). Furthermore, all fish treatments were reviewed
683 and approved in advance by the Ethics Committee at the TIGEM institute (Pozzuoli (NA), Italy).
684
685 **Ezrin$^{-/-}$ medaka generation by CRISPR/Cas9 system**
686 The genomic sequence of medaka *Ezrin* was obtained the medaka genome database at the Ensembl
687 Genome Database Project (http://www.ensembl.org/Oryzias_latipes; ENSORLG00000012128). Design
688 and construction of *OlEzrin*-sgRNA was committed to SYNTHEGO. The sequences of *OlEzrin*-

689 sgRNA oligonucleotides are listed in Table 1. Instead of Cas9 mRNA, the commercial reagent of
690 pCS2-nCas9n (Addgene, #4729) was used in this study. After pCS2-nCas9n was digested by NotI
691 treatment, this linearized vector was used as the template for synthesizing capped Cas9 mRNA with a
692 mMessage mMachine SP6 Kit (Life Technologies). Microinjection of the medaka embryos followed a
693 method described preciously by Kinoshita et al. (Kinoshita, Kani, Ozato, & Wakamatsu, 2000). A
694 mixture containing 200ng/μL of Cas9 mRNA and 20ng/μl of *OlEzrin*-sgRNA was prepared and
695 injected into the fertilized eggs at the one-cell stage. After hatching, the larvae were raised to sexual
696 maturity and used as "founder" fish (F0). To observe the genomic DNA mutations induced by Cas9
697 and *OlEzrin*-sgRNA in CRISPR/Cas9-mediated Ezrin-mutated medaka, a small piece of the caudal fin
698 from individual F0 fish was collected and subjected to genomic DNA analysis, using the primer set
699 indicating in Table 1. After the above screening had confirmed the occurrence of CRISPR/Cas9-
700 mediated Ezrin mutation in the F0 generation, these founder fish were crossed with each other, and
701 their offspring (F1) were checked for Ezrin mutations in the same way. Two of the F1 progeny with the
702 same mutation patterns were mated to produce the F2 generation. The F2 generation were crossed with
703 each other to produce F3 progeny, which was screened as described above to confirm that the same
704 mutation patterns were successfully inherited.
705

	Name	**Sequence (5'-3')**	**Usage**
EZRIN-gRNA	*olEzrin* Sense	ACAATGGATGAGCCTATTAG	CRISPR/Cas9-LoxP target site
	olEzrin Antisense	AGACTGATGCTGCCTCACTG	
Primers	*olEzrin*_Forward	GAACTCCTTCTAGCACCC	PCR for olEzrin

	*olEzrin*_Reverse	CCGCCTCCCTCCTCAATC	genotype

Table 1. Primer sequences.

Whole mount immunostaining

Medaka larvae were fixed in 4% PFA, 2X PBS, and 0.1% Tween-20. The fixed larvae were washed with PTW 1X and digested for 20 min with 10 µg/ml proteinase K and washed two-fold with 2 mg/ml glycine/PTW 1x. The samples were fixed for 20 min in 4% PFA, 2X PBS, and 0.1% Tween-20, washed with PTW 1X, and then incubated for 2 h in FBS 1%/PTW 1X, at room temperature. The larvae were incubated with mouse anti-EGFR (1:50, Santa Cruz sc-120) overnight at 4°C. The samples were washed with PTW 1X, incubated with the secondary antibody, Alexa-488 goat anti-mouse IgG (ThermoFisher), then with DAPI. Finally, the larvae were placed in glycerol 100%.

Statistical analysis

T-test, Welch's t-test, Mann-Whitney test. For the analysis of the statistically significant differences between two conditions, we performed the Shapiro-Wilk test to check if each condition had followed the normal distribution (null hypothesis): we performed the non-parametric Mann-Whitney test in case of rejection of the null hypothesis (p-value < 0.05), and we performed the parametric unpaired t-test in case of non-rejection of the null hypothesis (p-value ≥ 0.05). In the second case, we also performed the F-test to check the homoscedasticity between the compared conditions (null hypothesis): we applied the parametric Welch's t-test in case of rejection of the null hypothesis (p-value < 0.05). All the tests were performed with GraphPad Prism 10.0.0, GraphPad Software, Boston, Massachusetts USA.

ANOVA, Welch's ANOVA, Kruskal-Wallis test (with multiple comparisons post hoc tests). For the analysis of the statistically significant differences among multiple conditions, we performed the

Shapiro-Wilk test to check if each condition had followed the normal distribution (null hypothesis): we performed the non-parametric Kruskal-Wallis test in case of rejection of the null hypothesis (p-value < 0.05), and we performed the parametric one way ANOVA in case of non-rejection of the null hypothesis (p-value ≥ 0.05). In the second case, we also performed the Brown-Forsythe test to check the homoscedasticity between the compared conditions (null hypothesis): we applied the parametric Welch's one way ANOVA in case of rejection of the null hypothesis (p-value < 0.05). For completeness, we computed the p-values with post hoc tests for the pairwise multiple comparisons: Tukey's test for one way ANOVA, Dunnett's test for Welch's one way ANOVA, and Dunn's test for Kruskal-Wallis test. All the tests were performed with GraphPad Prism 10.0.0, GraphPad Software, Boston, Massachusetts USA.

Poisson Regression. For the analysis of the statically significant differences between two conditions with discrete values (i.e., counts), we performed the Poisson Regression over data, considering a Generalized Linear Model with Likelihood Ratio test. No correction for multiple comparisons was necessary. Poisson Regression with Generalized Linear Model and Likelihood Ratio test were performed with the package 'car' (version 3.1-2) in the R environment (version 4.2.3).

ACKNOWLEDGEMENTS

We are grateful to Dr. Cathal Wilson for critical reading and English editing of the manuscript. We are grateful to Edoardo Nusco for mice technical support. We also are grateful to Advanced Microscopy, Lysosomal Metabolism, Computational Biology and Medaka fish Cores at Department of Biology, University of studies of Naples Federico II. Acknowledgment is made to BioRender (www.biorender.com) for model images.

AUTHOR CONTRIBUTIONS

GG and DI performed the experiments and analyzed the data. DI and GG contributed to the experimental design, implementation, and interpretation. SB and FGS contributed to the technical part of the work. EDP and RDC performed bioinformatics analysis. EDP performed and supervised statistical evaluations. RDC and DA analyzed transcriptomics and proteomics data. BHM carried out domain-domain interaction analysis. FA and JM generated HeLa $EZR^{-/-}$ cells. MO and AE donated MEF EZR^{KO} cells. PG performed and analyzed mass spectrometry analysis. GG, DI and IC conceived the experiments, analyzed the data, and wrote the manuscript. All authors read and approved the final manuscript.

FUNDING

Work in the Conte group was supported by grants from the Million Dollar Bike Ride Grant Program MDBR-21-103-CHM, International Retinal Research Foundation, MIUR FISR2020IP_03551, MIUR PNRR_PRIN_P2022NPLZC, MIUR PRIN _2022WJFN5X,, and Sanfilippo Children's Foundations and National MPS Society.

REFERENCES

Abramson, J., Adler, J., Dunger, J., Evans, R., Green, T., Pritzel, A., . . . Jumper, J. M. (2024). Accurate structure prediction of biomolecular interactions with AlphaFold 3. *Nature, 630*(8016), 493-500. doi: 10.1038/s41586-024-07487-w

Antelmi, E., Cardone, R. A., Greco, M. R., Rubino, R., Di Sole, F., Martino, N. A., . . . Reshkin, S. J. (2013). ss1 integrin binding phosphorylates ezrin at T567 to activate a lipid raft signalsome driving invadopodia activity and invasion. *PLoS One, 8*(9), e75113. doi: 10.1371/journal.pone.0075113

Barroso-Gonzalez, J., Machado, J. D., Garcia-Exposito, L., & Valenzuela-Fernandez, A. (2009). Moesin regulates the trafficking of nascent clathrin-coated vesicles. *J Biol Chem, 284*(4), 2419-2434. doi: 10.1074/jbc.M805311200

Bolte, S., & Cordelieres, F. P. (2006). A guided tour into subcellular colocalization analysis in light microscopy. *J Microsc, 224*(Pt 3), 213-232. doi: 10.1111/j.1365-2818.2006.01706.x

Bonilha, V. L., Rayborn, M. E., Saotome, I., McClatchey, A. I., & Hollyfield, J. G. (2006). Microvilli defects in retinas of ezrin knockout mice. *Exp Eye Res, 82*(4), 720-729. doi: 10.1016/j.exer.2005.09.013

Borrelli, E., Sacconi, R., Zuccaro, B., Cavalleri, M., Bordato, A., Zucchiatti, I., . . . Querques, G. (2020). Photoreceptor alteration in intermediate age-related macular degeneration. *Sci Rep, 10*(1), 21036. doi: 10.1038/s41598-020-78201-9

Bulut, G., Hong, S. H., Chen, K., Beauchamp, E. M., Rahim, S., Kosturko, G. W., . . . Uren, A. (2012). Small molecule inhibitors of ezrin inhibit the invasive phenotype of osteosarcoma cells. *Oncogene, 31*(3), 269-281. doi: 10.1038/onc.2011.245

Burke, P., Schooler, K., & Wiley, H. S. (2001). Regulation of epidermal growth factor receptor signaling by endocytosis and intracellular trafficking. *Mol Biol Cell, 12*(6), 1897-1910. doi: 10.1091/mbc.12.6.1897

Carotenuto, P., Romano, A., Barbato, A., Quadrano, P., Brillante, S., Volpe, M., . . . Franco, B. (2022). Targeting the MITF/APAF-1 axis as salvage therapy for MAPK inhibitors in resistant melanoma. *Cell Rep, 41*(6), 111601. doi: 10.1016/j.celrep.2022.111601

Ceresa, B. P. (2012). Spatial regulation of epidermal growth factor receptor signaling by endocytosis. *Int J Mol Sci, 14*(1), 72-87. doi: 10.3390/ijms14010072

Cha, B., Tse, M., Yun, C., Kovbasnjuk, O., Mohan, S., Hubbard, A., . . . Donowitz, M. (2006). The NHE3 juxtamembrane cytoplasmic domain directly binds ezrin: dual role in NHE3 trafficking and mobility in the brush border. *Mol Biol Cell, 17*(6), 2661-2673. doi: 10.1091/mbc.e05-09-0843

Chirivino, D., Del Maestro, L., Formstecher, E., Hupe, P., Raposo, G., Louvard, D., & Arpin, M. (2011). The ERM proteins interact with the HOPS complex to regulate the maturation of endosomes. *Mol Biol Cell, 22*(3), 375-385. doi: 10.1091/mbc.E10-09-0796

Coscoy, S., Waharte, F., Gautreau, A., Martin, M., Louvard, D., Mangeat, P., . . . Amblard, F. (2002). Molecular analysis of microscopic ezrin dynamics by two-photon FRAP. *Proc Natl Acad Sci U S A, 99*(20), 12813-12818. doi: 10.1073/pnas.192084599

Di Malta, C., Zampelli, A., Granieri, L., Vilardo, C., De Cegli, R., Cinque, L., . . . Ballabio, A. (2023). TFEB and TFE3 drive kidney cystogenesis and tumorigenesis. *EMBO Mol Med, 15*(5), e16877. doi: 10.15252/emmm.202216877

Dibble, C. C., & Cantley, L. C. (2015). Regulation of mTORC1 by PI3K signaling. *Trends Cell Biol, 25*(9), 545-555. doi: 10.1016/j.tcb.2015.06.002

Dobin, A., Davis, C. A., Schlesinger, F., Drenkow, J., Zaleski, C., Jha, S., . . . Gingeras, T. R. (2013). STAR: ultrafast universal RNA-seq aligner. *Bioinformatics, 29*(1), 15-21. doi: 10.1093/bioinformatics/bts635

Edgar, R., Domrachev, M., & Lash, A. E. (2002). Gene Expression Omnibus: NCBI gene expression and hybridization array data repository. *Nucleic Acids Res, 30*(1), 207-210.

Gautreau, A., Poullet, P., Louvard, D., & Arpin, M. (1999). Ezrin, a plasma membrane-microfilament linker, signals cell survival through the phosphatidylinositol 3-kinase/Akt pathway. *Proc Natl Acad Sci U S A, 96*(13), 7300-7305. doi: 10.1073/pnas.96.13.7300

Haddad, L. A., Smith, N., Bowser, M., Niida, Y., Murthy, V., Gonzalez-Agosti, C., & Ramesh, V. (2002). The TSC1 tumor suppressor hamartin interacts with neurofilament-L and possibly functions as a novel integrator of the neuronal cytoskeleton. *J Biol Chem, 277*(46), 44180-44186. doi: 10.1074/jbc.M207211200

Huang da, W., Sherman, B. T., & Lempicki, R. A. (2009a). Bioinformatics enrichment tools: paths toward the comprehensive functional analysis of large gene lists. *Nucleic Acids Research, 37*(1), 1-13. doi: 10.1093/nar/gkn923

Huang da, W., Sherman, B. T., & Lempicki, R. A. (2009b). Systematic and integrative analysis of large gene lists using DAVID bioinformatics resources. *Nature Protocols, 4*(1), 44-57. doi: 10.1038/nprot.2008.211

Huang, J., Gu, S., Chen, M., Zhang, S. J., Jiang, Z., Chen, X., . . . Zhao, C. (2019). Abnormal mTORC1 signaling leads to retinal pigment epithelium degeneration. *Theranostics, 9*(4), 1170-1180. doi: 10.7150/thno.26281

Iwamatsu, T. (2004). Stages of normal development in the medaka Oryzias latipes. *Mech Dev, 121*(7-8), 605-618. doi: 10.1016/j.mod.2004.03.012

Kaur, G., & Lakkaraju, A. (2018). Early Endosome Morphology in Health and Disease. *Adv Exp Med Biol, 1074*, 335-343. doi: 10.1007/978-3-319-75402-4_41

Kawaguchi, K., & Asano, S. (2022). Pathophysiological Roles of Actin-Binding Scaffold Protein, Ezrin. *Int J Mol Sci, 23*(6). doi: 10.3390/ijms23063246

Kinoshita, M., Kani, S., Ozato, K., & Wakamatsu, Y. (2000). Activity of the medaka translation elongation factor 1alpha-A promoter examined using the GFP gene as a reporter. *Dev Growth Differ, 42*(5), 469-478. doi: 10.1046/j.1440-169x.2000.00530.x

Krishnan, K., Bruce, B., Hewitt, S., Thomas, D., Khanna, C., & Helman, L. J. (2006). Ezrin mediates growth and survival in Ewing's sarcoma through the AKT/mTOR, but not the MAPK, signaling pathway. *Clin Exp Metastasis, 23*(3-4), 227-236. doi: 10.1007/s10585-006-9033-y

Li, N., Kong, J., Lin, Z., Yang, Y., Jin, T., Xu, M., . . . Chen, L. (2019). Ezrin promotes breast cancer progression by modulating AKT signals. *Br J Cancer, 120*(7), 703-713. doi: 10.1038/s41416-019-0383-z

Lietha, D., Cai, X., Ceccarelli, D. F., Li, Y., Schaller, M. D., & Eck, M. J. (2007). Structural basis for the autoinhibition of focal adhesion kinase. *Cell, 129*(6), 1177-1187. doi: 10.1016/j.cell.2007.05.041

Liu, B., Chen, D., Chen, S., Saber, A., & Haisma, H. (2020). Transcriptional activation of cyclin D1 via HER2/HER3 contributes to EGFR-TKI resistance in lung cancer. *Biochem Pharmacol, 178*, 114095. doi: 10.1016/j.bcp.2020.114095

Liu, B., Chen, H., Johns, T. G., & Neufeld, A. H. (2006). Epidermal growth factor receptor activation: an upstream signal for transition of quiescent astrocytes into reactive astrocytes after neural injury. *J Neurosci, 26*(28), 7532-7540. doi: 10.1523/JNEUROSCI.1004-06.2006

Liu, S., Wang, Z., Zhu, R., Wang, F., Cheng, Y., & Liu, Y. (2021). Three Differential Expression Analysis Methods for RNA Sequencing: limma, EdgeR, DESeq2. *J Vis Exp*(175). doi: 10.3791/62528

Mitchell, D. C., Kuljanin, M., Li, J., Van Vranken, J. G., Bulloch, N., Schweppe, D. K., . . . Gygi, S. P. (2023). A proteome-wide atlas of drug mechanism of action. *Nat Biotechnol, 41*(6), 845-857. doi: 10.1038/s41587-022-01539-0

Muniz-Feliciano, L., Doggett, T. A., Zhou, Z., & Ferguson, T. A. (2017). RUBCN/rubicon and EGFR regulate lysosomal degradative processes in the retinal pigment epithelium (RPE) of the eye. *Autophagy, 13*(12), 2072-2085. doi: 10.1080/15548627.2017.1380124

Naso, F., Intartaglia, D., Falanga, D., Soldati, C., Polishchuk, E., Giamundo, G., . . . Conte, I. (2020). Light-responsive microRNA miR-211 targets Ezrin to modulate lysosomal biogenesis and retinal cell clearance. *EMBO J, 39*(8), e102468. doi: 10.15252/embj.2019102468

Nishimura, Y., Takiguchi, S., Ito, S., & Itoh, K. (2015). EGF□stimulated AKT activation is mediated by EGFR recycling via an early endocytic pathway in a gefitinib□resistant human lung cancer cell line. *Int J Oncol, 46*(4), 1721-1729. doi: 10.3892/ijo.2015.2871

Ognibene, M., Vanni, C., Segalerba, D., Mancini, P., Merello, E., Torrisi, M. R., . . . Eva, A. (2011). The tumor suppressor hamartin enhances Dbl protein transforming activity through interaction with ezrin. *J Biol Chem, 286*(34), 29973-29983. doi: 10.1074/jbc.M111.270785

Olsen, J. V., Blagoev, B., Gnad, F., Macek, B., Kumar, C., Mortensen, P., & Mann, M. (2006). Global, in vivo, and site-specific phosphorylation dynamics in signaling networks. *Cell, 127*(3), 635-648. doi: 10.1016/j.cell.2006.09.026

Ong, S. E., Blagoev, B., Kratchmarova, I., Kristensen, D. B., Steen, H., Pandey, A., & Mann, M. (2002). Stable isotope labeling by amino acids in cell culture, SILAC, as a simple and accurate

approach to expression proteomics. *Mol Cell Proteomics, 1*(5), 376-386. doi: 10.1074/mcp.m200025-mcp200

Oughtred, R., Rust, J., Chang, C., Breitkreutz, B. J., Stark, C., Willems, A., . . . Tyers, M. (2021). The BioGRID database: A comprehensive biomedical resource of curated protein, genetic, and chemical interactions. *Protein Sci, 30*(1), 187-200. doi: 10.1002/pro.3978

Palfy, M., Remenyi, A., & Korcsmaros, T. (2012). Endosomal crosstalk: meeting points for signaling pathways. *Trends Cell Biol, 22*(9), 447-456. doi: 10.1016/j.tcb.2012.06.004

Parameswaran, N., Enyindah-Asonye, G., Bagheri, N., Shah, N. B., & Gupta, N. (2013). Spatial coupling of JNK activation to the B cell antigen receptor by tyrosine-phosphorylated ezrin. *J Immunol, 190*(5), 2017-2026. doi: 10.4049/jimmunol.1201292

Petschnigg, J., Groisman, B., Kotlyar, M., Taipale, M., Zheng, Y., Kurat, C. F., . . . Stagljar, I. (2014). The mammalian-membrane two-hybrid assay (MaMTH) for probing membrane-protein interactions in human cells. *Nat Methods, 11*(5), 585-592. doi: 10.1038/nmeth.2895

Pettersen, E. F., Goddard, T. D., Huang, C. C., Meng, E. C., Couch, G. S., Croll, T. I., . . . Ferrin, T. E. (2021). UCSF ChimeraX: Structure visualization for researchers, educators, and developers. *Protein Sci, 30*(1), 70-82. doi: 10.1002/pro.3943

Pinelli, M., Carissimo, A., Cutillo, L., Lai, C. H., Mutarelli, M., Moretti, M. N., . . . di Bernardo, D. (2016). An atlas of gene expression and gene co-regulation in the human retina. *Nucleic Acids Res, 44*(12), 5773-5784. doi: 10.1093/nar/gkw486

Polishchuk, R. S., & Polishchuk, E. V. (2019). From and to the Golgi - defining the Wilson disease protein road map. *FEBS Lett, 593*(17), 2341-2350. doi: 10.1002/1873-3468.13575

Poupon, V., Stewart, A., Gray, S. R., Piper, R. C., & Luzio, J. P. (2003). The role of mVps18p in clustering, fusion, and intracellular localization of late endocytic organelles. *Mol Biol Cell, 14*(10), 4015-4027. doi: 10.1091/mbc.e03-01-0040

Rosset, C., Netto, C. B. O., & Ashton-Prolla, P. (2017). TSC1 and TSC2 gene mutations and their implications for treatment in Tuberous Sclerosis Complex: a review. *Genet Mol Biol, 40*(1), 69-79. doi: 10.1590/1678-4685-GMB-2015-0321

Salokas, K., Liu, X., Ohman, T., Chowdhury, I., Gawriyski, L., Keskitalo, S., & Varjosalo, M. (2022). Physical and functional interactome atlas of human receptor tyrosine kinases. *EMBO Rep, 23*(6), e54041. doi: 10.15252/embr.202154041

Saygideger-Kont, Y., Minas, T. Z., Jones, H., Hour, S., Celik, H., Temel, I., . . . Uren, A. (2016). Ezrin Enhances EGFR Signaling and Modulates Erlotinib Sensitivity in Non-Small Cell Lung Cancer Cells. *Neoplasia, 18*(2), 111-120. doi: 10.1016/j.neo.2016.01.002

Shang, P., Stepicheva, N., Teel, K., McCauley, A., Fitting, C. S., Hose, S., . . . Sinha, D. (2021). betaA3/A1-crystallin regulates apical polarity and EGFR endocytosis in retinal pigmented epithelial cells. *Commun Biol, 4*(1), 850. doi: 10.1038/s42003-021-02386-6

Sok, P., Gogl, G., Kumar, G. S., Alexa, A., Singh, N., Kirsch, K., . . . Remenyi, A. (2020). MAP Kinase-Mediated Activation of RSK1 and MK2 Substrate Kinases. *Structure, 28*(10), 1101-1113 e1105. doi: 10.1016/j.str.2020.06.007

Sorkin, A., & von Zastrow, M. (2009). Endocytosis and signalling: intertwining molecular networks. *Nat Rev Mol Cell Biol, 10*(9), 609-622. doi: 10.1038/nrm2748

Stanasila, L., Abuin, L., Diviani, D., & Cotecchia, S. (2006). Ezrin directly interacts with the alpha1b-adrenergic receptor and plays a role in receptor recycling. *J Biol Chem, 281*(7), 4354-4363. doi: 10.1074/jbc.M511989200

Tamma, G., Klussmann, E., Oehlke, J., Krause, E., Rosenthal, W., Svelto, M., & Valenti, G. (2005). Actin remodeling requires ERM function to facilitate AQP2 apical targeting. *J Cell Sci, 118*(Pt 16), 3623-3630. doi: 10.1242/jcs.02495

Tanaka, T., Zhou, Y., Ozawa, T., Okizono, R., Banba, A., Yamamura, T., . . . Sakurai, H. (2018). Ligand-activated epidermal growth factor receptor (EGFR) signaling governs endocytic trafficking of unliganded receptor monomers by non-canonical phosphorylation. *J Biol Chem, 293*(7), 2288-2301. doi: 10.1074/jbc.M117.811299

Toops, K. A., Tan, L. X., & Lakkaraju, A. (2014). A detailed three-step protocol for live imaging of intracellular traffic in polarized primary porcine RPE monolayers. *Exp Eye Res, 124*, 74-85. doi: 10.1016/j.exer.2014.05.003

Tsai, F. C., Bertin, A., Bousquet, H., Manzi, J., Senju, Y., Tsai, M. C., . . . Bassereau, P. (2018). Ezrin enrichment on curved membranes requires a specific conformation or interaction with a curvature-sensitive partner. *Elife, 7*. doi: 10.7554/eLife.37262

Vogel, G. F., Ebner, H. L., de Araujo, M. E., Schmiedinger, T., Eiter, O., Pircher, H., . . . Hess, M. W. (2015). Ultrastructural Morphometry Points to a New Role for LAMTOR2 in Regulating the Endo/Lysosomal System. *Traffic, 16*(6), 617-634. doi: 10.1111/tra.12271

Wan, X., Mendoza, A., Khanna, C., & Helman, L. J. (2005). Rapamycin inhibits ezrin-mediated metastatic behavior in a murine model of osteosarcoma. *Cancer Res, 65*(6), 2406-2411. doi: 10.1158/0008-5472.CAN-04-3135

Wang, Y., Pennock, S., Chen, X., & Wang, Z. (2002). Endosomal signaling of epidermal growth factor receptor stimulates signal transduction pathways leading to cell survival. *Mol Cell Biol, 22*(20), 7279-7290. doi: 10.1128/MCB.22.20.7279-7290.2002

Warde-Farley, D., Donaldson, S. L., Comes, O., Zuberi, K., Badrawi, R., Chao, P., . . . Morris, Q. (2010). The GeneMANIA prediction server: biological network integration for gene prioritization and predicting gene function. *Nucleic Acids Res, 38*(Web Server issue), W214-220. doi: 10.1093/nar/gkq537

Wee, P., & Wang, Z. (2017). Epidermal Growth Factor Receptor Cell Proliferation Signaling Pathways. *Cancers (Basel), 9*(5). doi: 10.3390/cancers9050052

Zhao, H., Shiue, H., Palkon, S., Wang, Y., Cullinan, P., Burkhardt, J. K., . . . Turner, J. R. (2004). Ezrin regulates NHE3 translocation and activation after Na+-glucose cotransport. *Proc Natl Acad Sci U S A, 101*(25), 9485-9490. doi: 10.1073/pnas.0308400101

Zhou, R., Cao, X., Watson, C., Miao, Y., Guo, Z., Forte, J. G., & Yao, X. (2003). Characterization of protein kinase A-mediated phosphorylation of ezrin in gastric parietal cell activation. *J Biol Chem, 278*(37), 35651-35659. doi: 10.1074/jbc.M303416200

Zhou, R., Zhu, L., Kodani, A., Hauser, P., Yao, X., & Forte, J. G. (2005). Phosphorylation of ezrin on threonine 567 produces a change in secretory phenotype and repolarizes the gastric parietal cell. *J Cell Sci, 118*(Pt 19), 4381-4391. doi: 10.1242/jcs.02559

Figure legends

Figure 1. **Deletion of Ezrin increases the lysosomal pathway. A,** Gene Ontology of 530 genes differentially expressed at mRNA and protein levels (EZR^{KO} versus WT). Bubble plot representing some of the most enriched GO terms regarding cellular components. Color and x axis represent minus logarithms of p Value. The size represents the numbers of genes enriched in a GO term. **B**, WT and EZR^{KO} MEF cells were cultured in 6-cm cell plates for 24 hours, then fixed and immunostained with

965 lysotracker and DAPI. Scale bar 10 µm. **C**, Data represent mean of lysotracker-positive cells ± SEM
966 (n=3 experiments at least). Statistical test: unpaired t-test. **D**, MEF cells WT and Ezr^{KO} were cultured in
967 6-well plates for 24 hours, then fixed and immunostained with LAMP1 and LC3 antibodies and DAPI.
968 Scale bar 10 µm (magnification 1 µm). **E**, Data represent mean of LAMP1-LC3 colocalization spots ±
969 SEM (n=3 experiments at least). Statistical test: unpaired t-test. **F,** Model showing autophagic flux
970 induction in $EZR^{-/-}$ cells. **G**, MEF Ezr^{KO} showed CTSB enzymatic activity increase compared to control
971 cells. **H**, MEF cells WT and Ezr^{KO} were lysed and immunoblotted with NBR1, LAMP1, EZR, P62,
972 LC3 antibodies or GAPDH antibodies as a loading control. The graphs show the mean NBR1, LAMP1,
973 EZR, P62, LC3 levels relative to GAPDH ± SEM (n=3 experiments at least). Statistical test: unpaired t-
974 test for NBR1, P62, LC3-I; Welch's t-test for CTSD, LC3-II; Mann-Whitney test for LAMP1.
975
976 **Figure 2. Ezrin binds EGFR and regulates its activation. A,** Bubble plot representing the
977 enrichment analysis of 530 DEGs performed in SILAC Phosphoproteomics data. Color and x axis
978 represent minus logarithms of p Value. The size represents numbers of genes enriched in the indicated
979 data. **B**, Physical interactions, obtained by GeneMANIA, highlight Ezrin and EGFR binding. **C**,
980 Volcano plot of DEGs, with up-regulated EGFR and down-regulated MAP2 and ERBB2 (no threshold
981 on Log2FC and 0.05 threshold on -Log10FDR). Legend: red dot, up-regulated gene; blue dot, down-
982 regulated gene; grey dot, not significant gene. **D,E** Co-IP data for Ezrin-EGFR interaction. For the co-
983 IP analyses, was used Ezrin antibody, conjugated with beads, and immunoblotted with EGFR antibody
984 for WT and $EZR^{-/-}$ (**D**) and HeLa EZR^{T567D} and EZR^{T567A} (**E**) HeLa cells, respectively. Schematic
985 representation of HeLa EZR^{T567D} and EZR^{T567A} co-IP (bottom). **F**, Confocal microscopy images
986 showing EGFR (green) and EZR (red) co-localization on the membrane in HeLa WT cells (left) and
987 magnified views of the regions are provided (right). Scale bar 10 µm (magnification 1 µm).
988 Representative plots of co-localization profiles on the membrane between EGFR (green) and EZR

(red). Data represent mean of EGFR-EZR colocalization spots ± SEM (n=3 experiments at least); **G**, Immunofluorescent labelling images of EGFR in HeLa WT and EZR$^{-/-}$ cells, observed by confocal microscopy. Scale bar 10 µm. **H**, Data represent fluorescence intensity ± SEM (n=3 experiments at least). Statistical test: unpaired t-test; **I**, Immunoblots and calculated levels (bottom) of HER3, pY845 EGFR, EGFR, pT222 MK2, MK2, pT180/pY182 p38 MAPK and P38 MAPK in HeLa WT and EZR$^{-/-}$ cells. Data are expressed as mean of pY845EGFR/EGFR, pT222 MK2/MK2 and pT180/pY182 p38 MAPK/P38 MAPK ratio ± SEM (n=3 experiments at least). GAPDH was used as loading control. Statistical test: unpaired t-test for pY845 EGFR; Mann-Whitney test for HER3, EGFR, pT222 MK2, pT180/pY182 p38 MAPK.

Figure 3. Ezrin controls EGFR localization. A, Western blot analysis of chemical crosslinked EGFR in HeLa WT and EZR$^{-/-}$ with (+) and without (-) EGF stimulation. Arrowheads indicate detected signals of dimeric and monomeric form of EGFR. **B**, Model showing the crosslinking effect of EGFR dimer formation in HeLa WT and EZR$^{-/-}$. **C**, Immunofluorescence images of EGFR (green) and EEA1 (red) in HeLa WT (top) and EZR$^{-/-}$ (bottom) observed by confocal microscopy. Scale bar 10 µm (magnification 1 µm). Representative plots of co-localization profiles of EGFR in early endosome. HeLa EZR$^{-/-}$ cells do not show EGFR and EEA1 co-localization compared to control cells. **D**, Data represent mean of EGFR-EEA1 colocalization spots ± SEM (n=3 experiments at least). Statistical test: unpaired t-test. **E**, Representative immunoblots of EGFR in membrane (top) and endosomes (bottom) proteins in HeLa WT and EZR$^{-/-}$. ZO-1 and EEA1 are used as membrane and endosomes extraction control, respectively. GAPDH are used as loading control. **F**, Schematic translocation of EGFR in the endosomes in HeLa WT compared to HeLa EZR$^{-/-}$. **G**, HeLa cells were fixed and immunostained with endotracker and EEA1 (red) and DAPI (blue). Scale bar 10 µm (magnification 1 µm). **H**, Graph shows mean of endotracker-positive cells ± SEM (n=3 experiments at least). Statistical test: unpaired t-test.

Figure 4. EGFR migrates on the endosomes depending on Ezrin. A, Immunofluorescence labelling images of EGFR-GFP (green), EEA1 (red) and DAPI (blue) after 3h of EGF stimulation (right) in HeLa WT (top) and $EZR^{-/-}$ (bottom). Magnified views of the regions in the boxes are provided in both Airyscan high-resolution microscopy and 3D-confocal microscopy. **B**, EGFR and EEA1 co-localization is expressed as a representative plot in HeLa WT (top) and $EZR^{-/-}$ (bottom). Scale bar 10 µm (magnification 1 µm). **C**, Data represent mean of EGFR-EEA1 colocalization spots ± SEM (n=3 experiments at least). Statistical test: One Way ANOVA.

Figure 5. EGF stimulation does not affect EGFR in absence of Ezrin. A, Live cell imaging and model for EGFR (green) translocation from the membrane to the endosomes in HeLa WT (top) and $EZR^{-/-}$ (bottom) cells without EGF stimulation (T0) and with a progressive EGF stimulation (from T10'' to T60''). White boxes are magnifications that depict EGFR protein migration. Scale bar 1 µm). Please refer to Video 1. **B**, IEM (anti-GFP immunolabelling) of cycloheximide treated HeLa WT, WT + EGF, $EZR^{-/-}$ and $EZR^{-/-}$ + EGF cells expressing EGFR-GFP. Endosomes containing EGFR is shown in green. Scale bar 200 nm. Quantitative analysis (right) of EGFR positive endosomes expressed as mean ± SEM. Statistical test: generalized Linear Model with Likelihood Ratio (Poisson Regression). **C**, immunoblots and calculated levels (bottom) of HER2, pY845 EGFR, pY1068 EGFR, EGFR, pT202/Y204 p42/44 MAPK, pT180/pY182 p38 MAPK and P38 MAPK in HeLa WT and $EZR^{-/-}$ cells with (+) and without (-) EGF stimulation. Data are expressed as mean of pY845EGFR/EGFR and pT180/pY182 p38 MAPK/P38 MAPK ratio ± SEM (n=3 experiments at least). GAPDH was used as loading control. Statistical test: Unpaired t-test for HER2 WT, HER2 $EZR^{-/-}$, pY845 EGFR $EZR^{-/-}$, pY1068 EGFR WT, pY1068 EGFR $EZR^{-/-}$, EGFR WT, EGFR $EZR^{-/-}$, pT202/Y204 p44/42 MAPK WT, pT202/Y204 p44/42 MAPK $EZR^{-/-}$, pT180/pY182 p38 MAPK WT, pT180/pY182 p38 MAPK

EZR$^{-/-}$; unpaired t-test with Welch's correction for pY845 EGFR WT. **D**, Representative immunoblots of EGFR in membrane (top) and endosomes (bottom) proteins in HeLa WT and EZR$^{-/-}$ with (+) and without (-) EGF stimulation. ZO-1 and EEA1 are used as membrane and endosomes extraction control, respectively. GAPDH are used as loading control.

Figure 6. EGFR-Ezrin complex interacts with TSC1. A, co-IP analysis for Ezr-TSC1 (left) and EGFR-TSC1 (right) interaction. For co-IP analyses, Ezrin (left) and EGFR (right) antibodies were used. The proteins immunoprecipitated were blotted for TSC1 and AKT antibodies in HeLa WT and EZR$^{-/-}$. **B**, HeLa WT and EZR$^{-/-}$ cells were lysed and immunoblotted with pS939 TSC2, TSC2, PT389 P70 S6 Kinase, P70 S6 Kinase, pS473 AKT, AKT, pS65 4E-BP1, 4E-BP1 and GAPDH as a loading control. Data represent the mean of pS939 TSC2/TSC2, T389 P70 S6 Kinase/P70 S6 Kinase, pS473 AKT/AKT and pS65 4E-BP1/4E-BP1 ratio ± SEM (n=3 experiments at least). Statistical test: unpaired t-test for pT389 P70 S6 Kinase, pS473 AKT; Unpaired t-test with Welch's correction for pS939 TSC2; Mann-Whitney test for pS939 TSC2. **C**, pP70 S6 Kinase western blotting with insulin time course in HeLa WT (up) and EZR$^{-/-}$ (bottom) cells. Graph shows the mean of pP70 S6/P70 S6 ratio ± SEM (n=3 experiments at least). Statistical test: One Way ANOVA for WT and KO curve (pairwise comparisons with reference T0). **D**, Representative confocal images of LAMP1 and TSC1 (left) and LAMP1 and TSC2 (right) immunofluorescence in HeLa WT and EZR$^{-/-}$ cells. Magnified insets of TSC1/2 localization are shown. Scale bar 10 µm (magnification 1 µm). **E**, Data represent mean of LAMP1-TSC1 (left) and LAMP1-TSC2 (right) colocalization spots ± SEM (n=3 experiments at least). Statistical test: unpaired t-test for LAMP1-TSC1; Unpaired t-test with Welch's correction for LAMP1-TSC2. **F**, pS473 AKT western blotting with EGF time course in HeLa WT (left) and EZR$^{-/-}$ (right) cells. Graph shows the mean of pS473 AKT/AKT ratio ± SEM (n=3 experiments at least). Statistical test: One Way ANOVA with Dunnett's post-hoc test for WT curve; Kruskal-Wallis test with Dunn's

post-hoc test for KO curve (pairwise comparisons with reference T0). NS: not significant. **G**, HeLa WT, WT + EGF, $EZR^{-/-}$ and $EZR^{-/-}$ + EGF cells were immunostained with EGFR (green), TSC1 (red) and EEA1 (gray). Representative magnifications are shown. Scale bar 10 µm (magnification 1 µm). **H**, Data represent mean of TSC1-EEA1 colocalization spots ± SEM (n=3 experiments at least). Statistical test: One Way ANOVA.

Figure 7. *Ezrin* depletion induces EGFR-mediated retinal degeneration. A, Schematic representation of used CRISPR/Cas9 strategy to generate $Ezrin^{-/-}$ medaka lines. The red box highlighted the deleted nucleotides in the *Ezrin* exon 1 gene. **B**, WT and $Ezrin^{-/-}$ medaka proteins were immunoblotted with Ezrin antibody and Actin as a loading control. **C**, Stereo-microscopic representative images of WT and $Ezrin^{-/-}$ medaka at stage 40. Scale bar 1 mm. **D**, Immunoblots and calculated levels (right) of pT1462 TSC2, pS473 Akt, LC3-I, LC3-II, pY845 Egfr and Egfr, pS65 4E-BP1 in WT and $Ezrin^{-/-}$ medaka fish. Data are expressed as mean of pT1462 TSC2/TSC2, pS473 Akt/Akt, pS65 4E-BP1/4EB-P1 and pY845EGFR/EGFR ratio ± SEM (n=3 experiments at least). Actin was used as loading control. Statistical test: Unpaired t-test. **E**, Representative confocal images of LAMP1 immunofluorescence in WT and $Ezrin^{-/-}$ medaka fish. Magnified insets of RPE LAMP1 localization are shown. Scale bar 10 µm. RPE: retinal pigment epithelium; ONL: outer nuclear layer; INL: inner nuclear layer. **F**, Medaka WT and $Ezrin^{-/-}$ fish were immunostained with EGFR. Scale bar 10 µm. **G**, Immunofluorescence labelling images of RHO (left) and ZPR1 (right) in WT and $Ezrin^{-/-}$ fish. Magnified views of the regions in the boxes are provided at the bottom. Scale bar 10 µm. **H,** Confocal images showing representative TUNEL positive cells on cryosection from WT and $Ezrin^{-/-}$ medaka lines. Scale bar 10 µm. Graph shows the mean of number of TUNEL positive cells for retina ± SEM (n=3 experiments at least). Statistical test: unpaired t-test.

Figure 8. EGFR/Ezrin/TSC complex molecular pathway

Diurnal inactivation of Ezrin leads to incapacity of EGFR to dimerize. The absence of active EGFR on the endosome causes the migration of TSC complex on the lysosome, where it inhibits mTORC1C1. On the contrary, the nocturnal activation of Ezrin favorites the phosphorylation and dimerization of EGFR, that translocate from the plasma membrane on the early endosome. Ezrin localized with EGFR, on the endosomal membrane, binds TSC complex, preventing mTORC1C1 inactivation on the lysosome.

Figure supplement 1. **Ezrin knockout cells show lysosomal enhancement. A,** VENN diagram showing the comparison of transcriptomics (GSE195983) and proteomics (PRIDE ID: PXD045157) performed in EZR^{KO} MEF cells. 572 genes are commonly regulated: 317 and 213 genes are induced and inhibited in both datasets, respectively; the remaining 42 are regulated in opposite manner. Heatmap on 22 Lysosomal genes (out of 317) induced in the transcriptome **B** and in the proteome **C**. **D,** Schematic representation of *Ezrin* gene and the corresponding protein. The position of the mutation in exon 2 and the relative changes in the coding sequence is highlighted. **E,** WT and $EZR^{-/-}$ HeLa cells were cultured in 6-cm cell plates for 24 hours, then fixed and immunostained with lysotracker and DAPI. Scale bar 10 µm. **F,** Data represent mean of lysotracker-positive cells ± SEM (n=3 experiments at least). Statistical test: unpaired t-test. **G,** HeLa WT and $EZR^{-/-}$ cells were lysed and immunoblotted with NBR1, LAMP1, EZR, p62, LC3 antibodies or GAPDH antibody as a loading control. Data represent the mean relative NBR1, LAMP1, p62 and LC3 levels relative to GAPDH ± SEM (n=3 experiments at least). Statistical test: unpaired t-test for NBR1, p62, LC3-I and LC3-II; Mann-Whitney test for LAMP1. **H,** HeLa $EZR^{-/-}$ showed CTSB enzymatic activity increase compared to control cells. Statistical test: unpaired t-test. **I,** HeLa WT and $EZR^{-/-}$ cells were cultured in normal medium (stv-, baf-). Starved HBSS medium (stv+), or starved medium supplemented with bafilomycin (baf+) or without

bafilomycin (baf-), were lysed and immunoblotted with LC3 antibodies or GAPDH antibody as a loading control. Data represent the mean relative LC3 levels relative to GAPDH ± SEM (n=3 experiments at least). Statistical test: unpaired t-test for all the comparisons against WT; Mann-Whitney test for all the comparisons against $EZR^{-/-}$. **J**, Immunofluorescence labelling images of TFEB-GFP (green) in WT and $EZR^{-/-}$ HeLa cells. Scale bar 50 µm.

Figure supplement 2. E**zrin genetic and pharmacological depletion causes EGFR signaling alteration. A** and **B,** Bubble plots representing the enrichment analysis of 530 DEGs performed in kinase perturbation from GEO database and from the Proteomics Drug Atlas. Color and x axis represent minus logarithms of p Value. The size represents numbers of genes enriched in the indicated data. **C**, Domain interaction network based on multiple resources. Proteins are colored shapes; domains are dots. Domains are connected if they are found in a reliable association within a database/resource, with color coding the database/resource. **D,** MEF cells were fixed and immunostained with endotracker (red) and DAPI (blue). Scale bar 10 µm. **E**, Graph shows mean of endotracker-positive cells ± SEM (n=3 experiments at least). Statistical test: unpaired t-test. **F,** Immunoblots and calculated levels (bottom) of HER2, HER3, EGFR, pT222 MK2, MK2, pT202/Y204 P44/42 MAPK, P44/42 MAPK, pT180/pY182 p38 MAPK and P38 MAPK in MEF WT and EZR^{KO} cells. Data are expressed as mean of HER2, HER3, EGFR, pT222 MK2/MK2, pT202/Y204 P44/42 MAPK/P44/42 MAPK and pT180/pY182 p38 MAPK/ p38 MAPK ratio ± SEM (n=3 experiments at least). GAPDH was used as loading control. Statistical test: unpaired t-test for HER3 and pT180/pY182 p38 MAPK; unpaired t-test with Welch's correction for EGFR; Mann-Whitney test for HER2 and pT222 MK2. **G,** Representative immunoblots of EGFR in endosomes proteins in MEF WT and EZR^{KO}. EEA1 are used as endosomes extraction control. **H,** Immunofluorescence images of EGFR (green) and EEA1 (red) in MEF WT and EZR^{KO} observed by confocal microscopy. Scale bar 10 µm (magnification 1 µm).

Figure supplement 3. EZRIN interacts with TSC1.

A, Immunoblots and calculated levels (bottom) of HER2, HER3, pY845 EGFR, EGFR, pT222 MK2, MK2, pT180/pY182 p38 MAPK and P38 MAPK in MEF WT and EZR^{KO} cells. Data are expressed as mean of HER2, HER3, pY845 EGFR, EGFR, pT222 MK2 and pT180/pY182 p38 MAPK ratio ± SEM (n=3 experiments at least). GAPDH was used as loading control. Data are expressed as mean of HER2, HER3, pY845EGFR/EGFR, EGFR, pT222 MK2/MK2 and pT180/pY182 p38 MAPK/P38 MAPK ratio ± SEM (n=3 experiments at least). Statistical test: One Way ANOVA with Tukey's post-hoc test for HER2, EGFR, pT222 MK2 and pT180/pY182 p38 MAPK; Kruskal-Wallis test with Dunn's post-hoc for pY845 EGFR. **B,** Immunofluorescence labelling images of EGFR-GFP (green), EEA1 (red) and DAPI (blue) after 3h of EGF stimulation (bottom) in HeLa WT (left) and *NSC668394*-treated cells (right). Scale bar 10 µm (magnification 1 µm). **C-E**, Alphafold3 fold prediction for the EZRIN (UID:P15311)/HAMARTIN (UID:Q92574) dimer and detail of domain-domain interaction (**F-H**). The dimer prediction is color-coded by chain (**C**; EZRIN is firebick, HAMARTIN is orange), by plddt (**D**; yellow to blue with blue better), and by domain (cyan is hamartin protein domain (PF04388), magenta is FERM C-terminal PH-like domain (PF09380), green is FERM N-terminal domain (PF09379)). (**E,F**) closeup of the interface as surface (**F**) and spheres representation (**G**). (**H**) is the structural alignment (ChimeraX mmaker) of the five dimer fold models over the hamartin protein domain. The stable portion (gray section) of hamartin is coloured in shades of blue, unreliable prediction (azure section) is depicted as gray sticks, FERM N and C term domain are depicted as ribbons and color-coded as per other subfigures. Regardless of the model confidence, EZRIN consistently interacts with a specific region of hamartin through FERM N/C domains. **J,** Immunofluorescence labelling images of LAMP1 (red), TSC1 (green) and DAPI (blue) after 30 min of Insulin stimulation (upper panel) and LAMP1

(red), TSC2 (green) and DAPI (blue) after 30 min of Insulin stimulation (lower panel) in HeLa WT and $EZR^{-/-}$ cells, respectively. Scale bar 10 µm (magnification 1 µm).

Figure supplement 4. **Ezrin inhibition induces mTORC1C1 pathway inhibition**. **A,** Immunoblots and calculated levels (bottom) of pS939 TSC2, TSC2, pT389 P70 S6 Kinase, P70 S6 Kinase, pS473 AKT, AKT, pS65 4E-BP1, 4E-BP1 in HeLa WT, DMSO-treated and *NSC668394*-treated cells. Data are expressed as mean of pS939 TSC2/TSC2, pT389 P70 S6 Kinase/P70 S6 Kinase, pS473 AKT/ AKT and pS65 4E-BP1/4E-BP1 ratio ± SEM (n=3 experiments at least). GAPDH was used as loading control. Statistical test: One Way ANOVA with Tukey's post-hoc test for pS939 TSC2, pS473 AKT, pS65 4E-BP1; Kruskal-Wallis test with Dunn's post-hoc test for pT389 P70 S6 Kinase. **B,** Immunoblots and calculated levels (bottom) of pT1462 TSC2, TSC2, pT389 P70 S6 Kinase, P70 S6 Kinase, pS473 AKT, AKT, pS65 4E-BP1 and 4E-BP1 in HeLa WT, DMSO-treated and *NSC668394*-treated cells. Data are expressed as mean of pT1462 TSC2/TSC2, pT389 P70 S6 Kinase/P70 S6 Kinase, pS473 AKT/ AKT and pS65 4E-BP1/4E-BP1 ratio ± SEM (n=3 experiments at least). GAPDH was used as loading control. Statistical test: One Way ANOVA with Tukey's post-hoc test for pT389 P70 S6 Kinase, pS473 AKT, pS65 4E-BP1; Kruskal-Wallis test with Dunn's post-hoc test for pT1462 TSC2. **C,** Immunofluorescence labelling images of LAMP1 (red), TSC1/TSC2 (green) and DAPI (blue) in MEF WT (left) and *NSC668394*-treated cells. Scale bar 10 µm (magnification 1 µm). **D,** Immunoblots and calculated levels (bottom) of pS939 TSC2, TSC2, pT389 P70 S6 Kinase, P70 S6 Kinase, pS473 AKT and AKT in MEF WT and EZR^{KO} cells. Data are expressed as mean of pS939 TSC2/TSC2, pT389 P70 S6 Kinase/P70 S6 Kinase and pS473 AKT/ AKT ratio ± SEM (n=3 experiments at least). GAPDH was used as loading control. Statistical test: unpaired t-test. **E,** Immunofluorescence labelling images of LAMP1 (red), TSC1 (green) and DAPI (blue) in MEF WT and EZR^{KO} cells. Scale bar 10 µm (magnification 1 µm). **F**, Immunoblots and calculated levels (right)

of pT389 P70 S6 Kinase in MEF WT, MEF WT with *NSC668394* treatment and TSC2^{KO} treated with *NSC668394* cells. Data are expressed as mean of pT389 P70 S6 Kinase/P70 S6 Kinase ratio ± SEM (n=3 experiments at least). GAPDH was used as loading control. Statistical test:one way ANOVA.

Figure supplement 5. Ezrin overexpression rescue EGFR and TSC1 localization. A, Immunofluorescence labelling images of EGFR-GFP (green), EZR^{T567D}-CHE (top), EZR^{T567A}-CHE (bottom), EEA1 (gray) and DAPI (blue) in HeLa EZR$^{-/-}$. EZR^{T567D}, but not EZR^{T567A}, with EGF stimulation rescued EGFR translocation on the endosomes in EZR$^{-/-}$ cells. Magnified views of EGFR and Ezrin localization are provided in both Airyscan high-resolution microscopy and 3D-confocal microscopy. Scale bar 10 µm (magnification 1 µm). **B**, Representative confocal images of EGFR-GFP (green), EZR^{T567D}-CHE (top), EZR^{T567A}-CHE (bottom), TSC1 (gray) and DAPI (blue) in HeLa EZR$^{-/-}$. TSC1 localization misplaced from lysosomes to endosomes in HeLa EZR$^{-/-}$ cells, after EZR^{T567D} transfection and upon EGF stimulation. Boxes show magnifications of TSC1 position, displayed both as Airyscan high-resolution microscopy and 3D-confocal microscopy. Scale bar 10 µm (magnification 1 µm).

Figure supplement 6. **Light/dark transitions regulate EGFR and mTORC11 signaling in mice RPE. A**, WT mice were exposed 3h in light on (left) and dark (right) condition and after 3 h the retina was analyzed by EGFR immunofluorescence. Representative images are shown. Scale bar 50 µm. Schematic summary of EGFR and Ezrin trend in mice retina. **B**, WT mice RPE were analyzed by western blot for EGFR pathway in light and dark conditions. Data are expressed as mean of pY845 EGFR/EGFR and pT180/pY182 p38 MAPK/P38 MAPK ratio ± SEM (n=3 experiments at least). GAPDH was used as loading control. Statistical test: unpaired t-test for EGFR, pY845 EGFR, and pT180/pY182 p38 MAPK. **C,** Immunoblots and calculated levels (right) of pS939 TSC2, TSC2, pT389

P70 S6 Kinase, P70 S6 Kinase, pS473 AKT, AKT, pT37/46 4E-BP1 and 4E-BP1 in light and dark-exposed WT mice. Data are expressed as mean of pS939 TSC2/TSC2, pT389 P70 S6 Kinase/P70 S6 Kinase, pS473 AKT/ AKT and pT37/46 4E-BP1/4E-BP1 ratio ± SEM (n=3 experiments at least). GAPDH was used as loading control. Statistical test: unpaired t-test for pS939 TSC2, pS473 AKT; Unpaired t-test with Welch's correction for pT389 P70 S6 Kinase; Mann-Whitney test for pT37/46 4E-BP1.

Video 1

WT HeLa cells expressing EGFR-GFP were imaged by TIRF super-resolution microscopy every were imaged every 0.5□s for 5 min after EGF stimulation (related to Figure 5A).

Video 2

Magnification from WT HeLa cells expressing EGFR-GFP, imaged by TIRF super-resolution microscopy every were imaged every 0.5□s for 5 min after EGF stimulation (related to Figure 5A).

Video 3

EZR$^{-/-}$ HeLa cells expressing EGFR-GFP were imaged by TIRF super-resolution microscopy every were imaged every 0.5□s for 5 min after EGF stimulation (related to Figure 5A).

Video 4

Magnification from EZR$^{-/-}$ HeLa cells expressing EGFR-GFP, imaged by TIRF super-resolution microscopy every were imaged every 0.5□s for 5 min after EGF stimulation (related to Figure 5A).

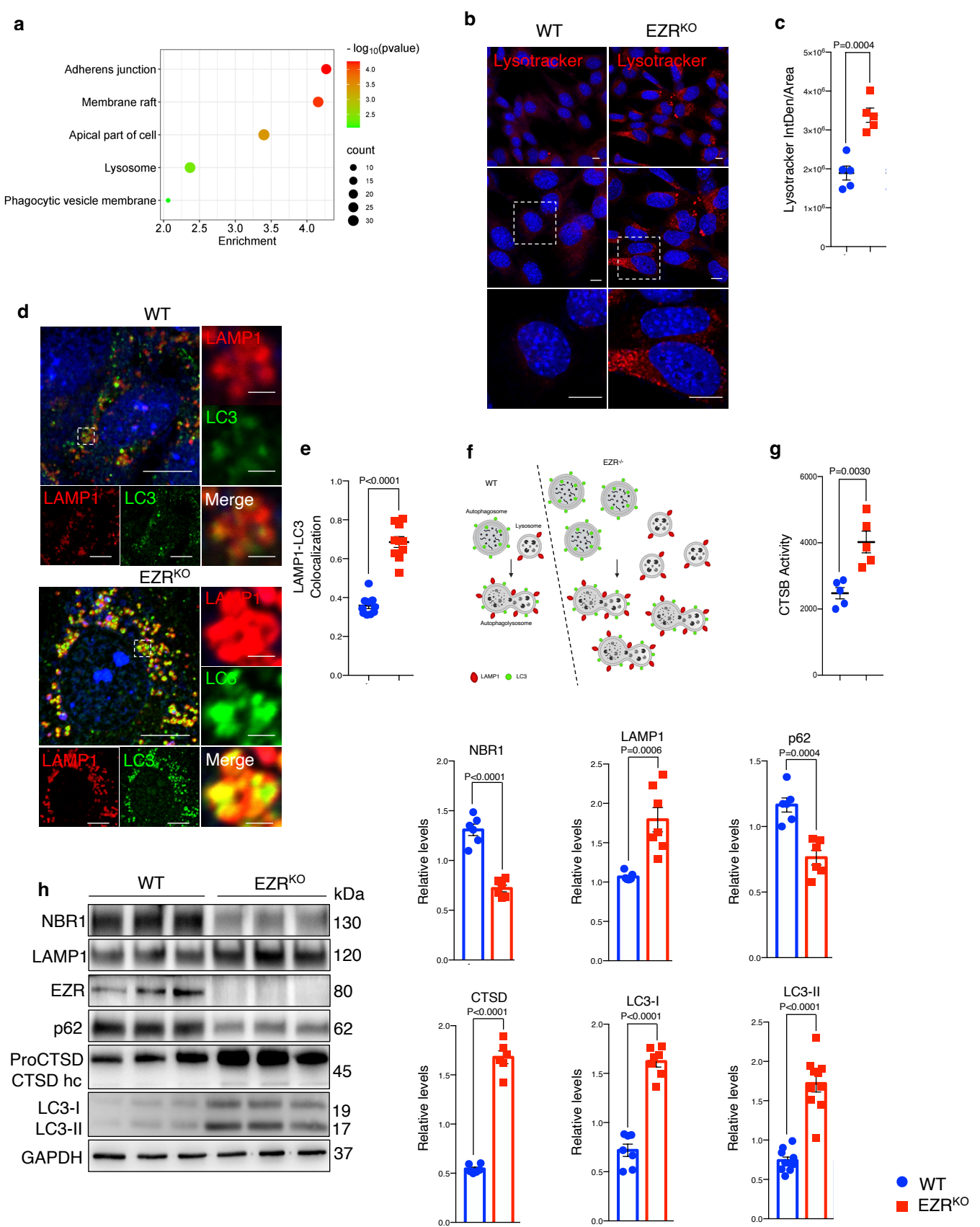
a
Adherens junction
Membrane raft
Apical part of cell
Lysosome
Phagocytic vesicle membrane
2.0
2.5
3.0
3.5
4.0
Enrichment
- log10(pvalue)
4.0
3.5
3.0
2.5
count
10
15
20
25
30
b
WT
EZRKO
Lysotracker
Lysotracker
c
P=0.0004
Lysotracker IntDen/Area
5x10^6
4x10^6
3x10^6
2x10^6
1x10^6
0
d
WT
LAMP1
LC3
LAMP1
LC3
Merge
EZRKO
LAMP1
LC3
LAMP1
LC3
Merge
e
P<0.0001
LAMP1-LC3 Colocalization
1.0
0.8
0.6
0.4
0.2
0.0
f
WT
EZR-/-
Autophagosome
Lysosome
Autophagolysosome
LAMP1
LC3
g
P=0.0030
CTSB Activity
6000
4000
2000
0
h
WT
EZRKO
kDa
NBR1
LAMP1
EZR
p62
ProCTSD
CTSD hc
LC3-I
LC3-II
GAPDH
130
120
80
62
45
19
17
37
NBR1
P<0.0001
LAMP1
P=0.0006
p62
P=0.0004
CTSD
P<0.0001
LC3-I
P<0.0001
LC3-II
P<0.0001
Relative levels
WT
EZRKO

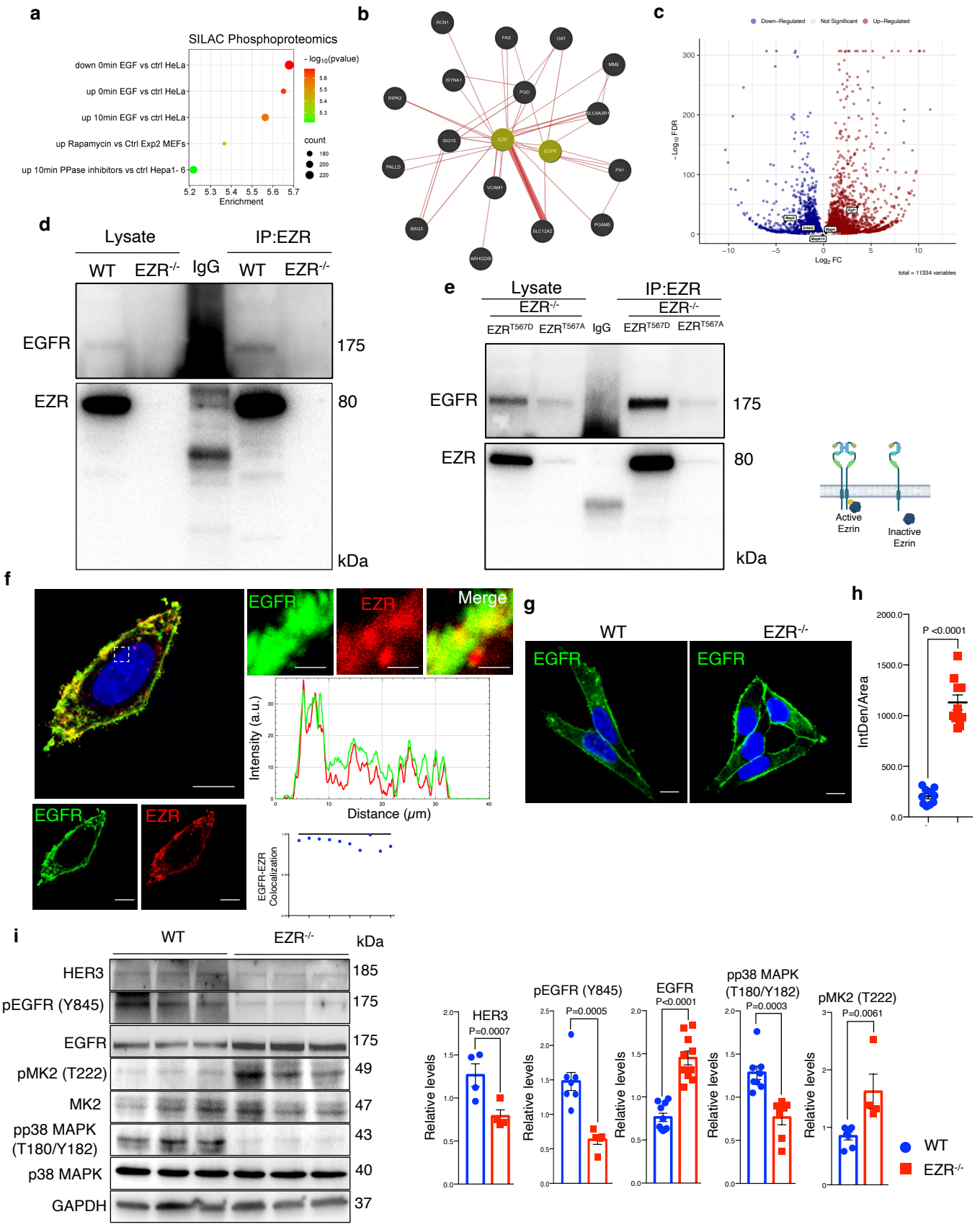
a
SILAC Phosphoproteomics
down 0min EGF vs ctrl HeLa
up 0min EGF vs ctrl HeLa
up 10min EGF vs ctrl HeLa
up Rapamycin vs Ctrl Exp2 MEFs
up 10min PPase inhibitors vs ctrl Hepa1- 6
- log10(pvalue)
count
Enrichment
b
RCN1
FAS
OAT
MME
ISYNA1
PGD
RIPK2
SLC9A3R1
ISG15
EZR
EGFR
PALLD
FN1
VCAM1
BAG3
SLC12A2
PGAM5
ARHGDIB
c
Down−Regulated
Not Significant
Up−Regulated
−Log10 FDR
Log2 FC
total = 11334 variables
d
Lysate
IP:EZR
WT
EZR-/-
IgG
WT
EZR-/-
EGFR
EZR
175
80
kDa
e
Lysate
IP:EZR
EZR-/-
EZR-/-
EZRT567D
EZRT567A
IgG
EZRT567D
EZRT567A
EGFR
EZR
175
80
kDa
Active Ezrin
Inactive Ezrin
f
EGFR
EZR
Merge
Intensity (a.u.)
Distance (μm)
EGFR
EZR
EGFR-EZR Colocalization
g
WT
EZR-/-
EGFR
EGFR
h
IntDen/Area
P <0.0001
i
WT
EZR-/-
kDa
HER3
pEGFR (Y845)
EGFR
pMK2 (T222)
MK2
pp38 MAPK (T180/Y182)
p38 MAPK
GAPDH
185
175
175
49
47
43
40
37
HER3
P=0.0007
pEGFR (Y845)
P=0.0005
EGFR
P<0.0001
pp38 MAPK (T180/Y182)
P=0.0003
pMK2 (T222)
P=0.0061
Relative levels
WT
EZR-/-

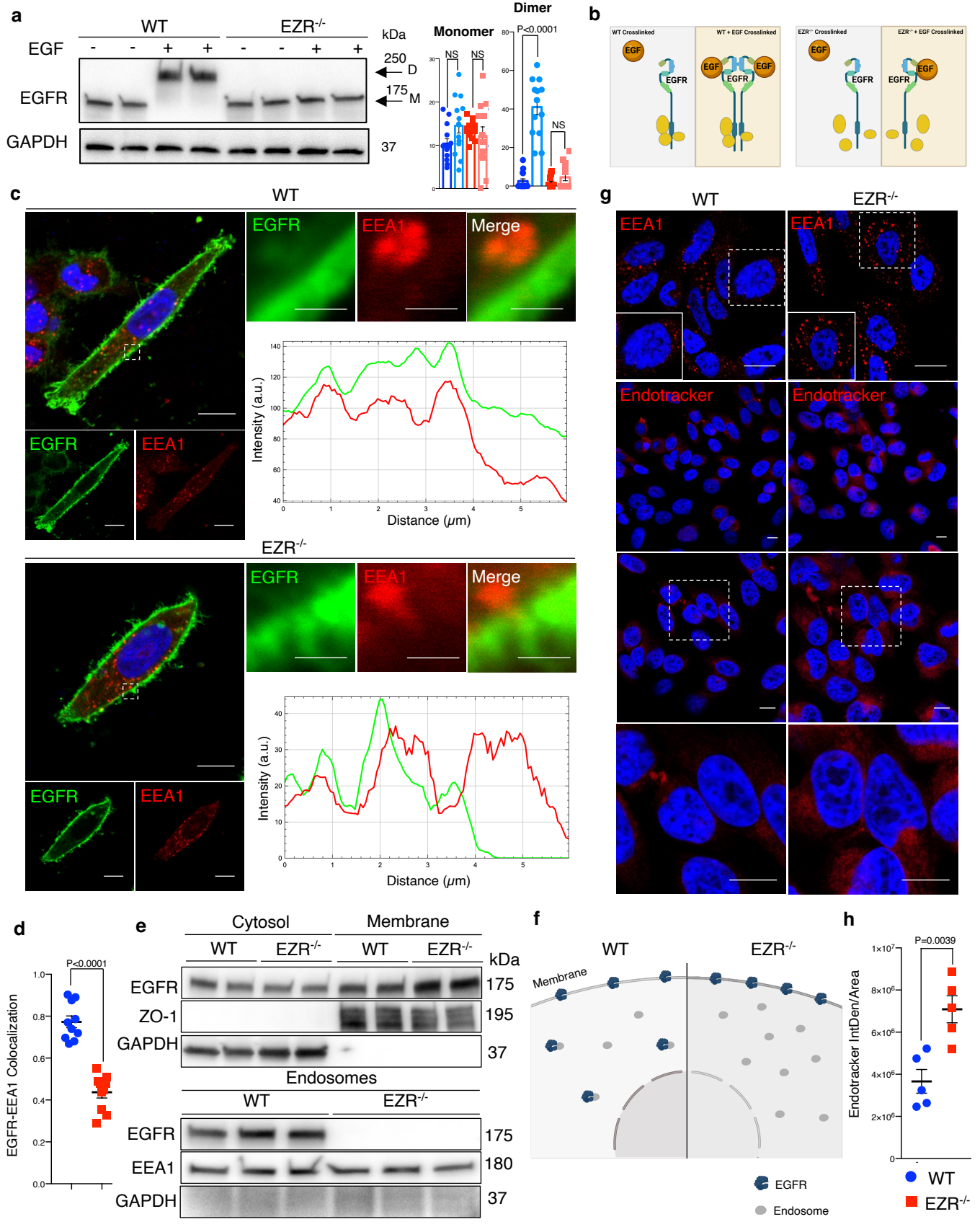
a
WT
EZR-/-
EGF
EGFR
GAPDH
kDa
250
D
175
M
37
Monomer
Dimer
NS
P<0.0001
b
WT Crosslinked
WT + EGF Crosslinked
EZR-/- Crosslinked
EZR-/- + EGF Crosslinked
EGF
EGFR
c
WT
EGFR
EEA1
Merge
Intensity (a.u.)
Distance (μm)
EZR-/-
g
WT
EZR-/-
EEA1
Endotracker
d
EGFR-EEA1 Colocalization
P<0.0001
e
Cytosol
Membrane
WT
EZR-/-
kDa
EGFR
ZO-1
GAPDH
175
195
37
Endosomes
EEA1
180
f
Membrane
Endosome
h
Endotracker IntDen/Area
P=0.0039

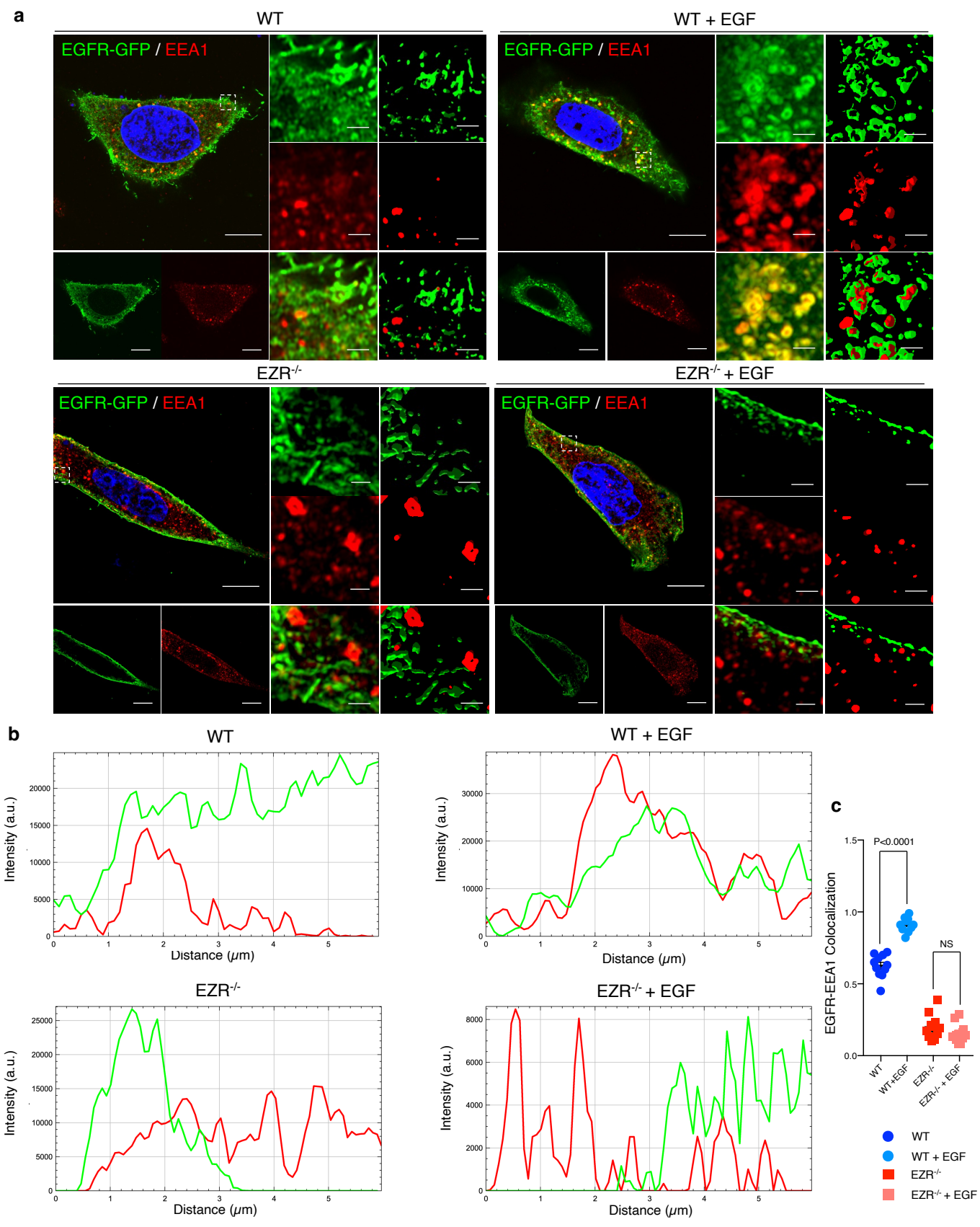
a
WT
EGFR-GFP / EEA1
WT + EGF
EGFR-GFP / EEA1
EZR-/-
EGFR-GFP / EEA1
EZR-/- + EGF
EGFR-GFP / EEA1
b
WT
Intensity (a.u.)
Distance (μm)
WT + EGF
Intensity (a.u.)
Distance (μm)
EZR-/-
Intensity (a.u.)
Distance (μm)
EZR-/- + EGF
Intensity (a.u.)
Distance (μm)
c
P<0.0001
NS
EGFR-EEA1 Colocalization
WT
WT+EGF
EZR-/-
EZR-/- + EGF
WT
WT + EGF
EZR-/-
EZR-/- + EGF

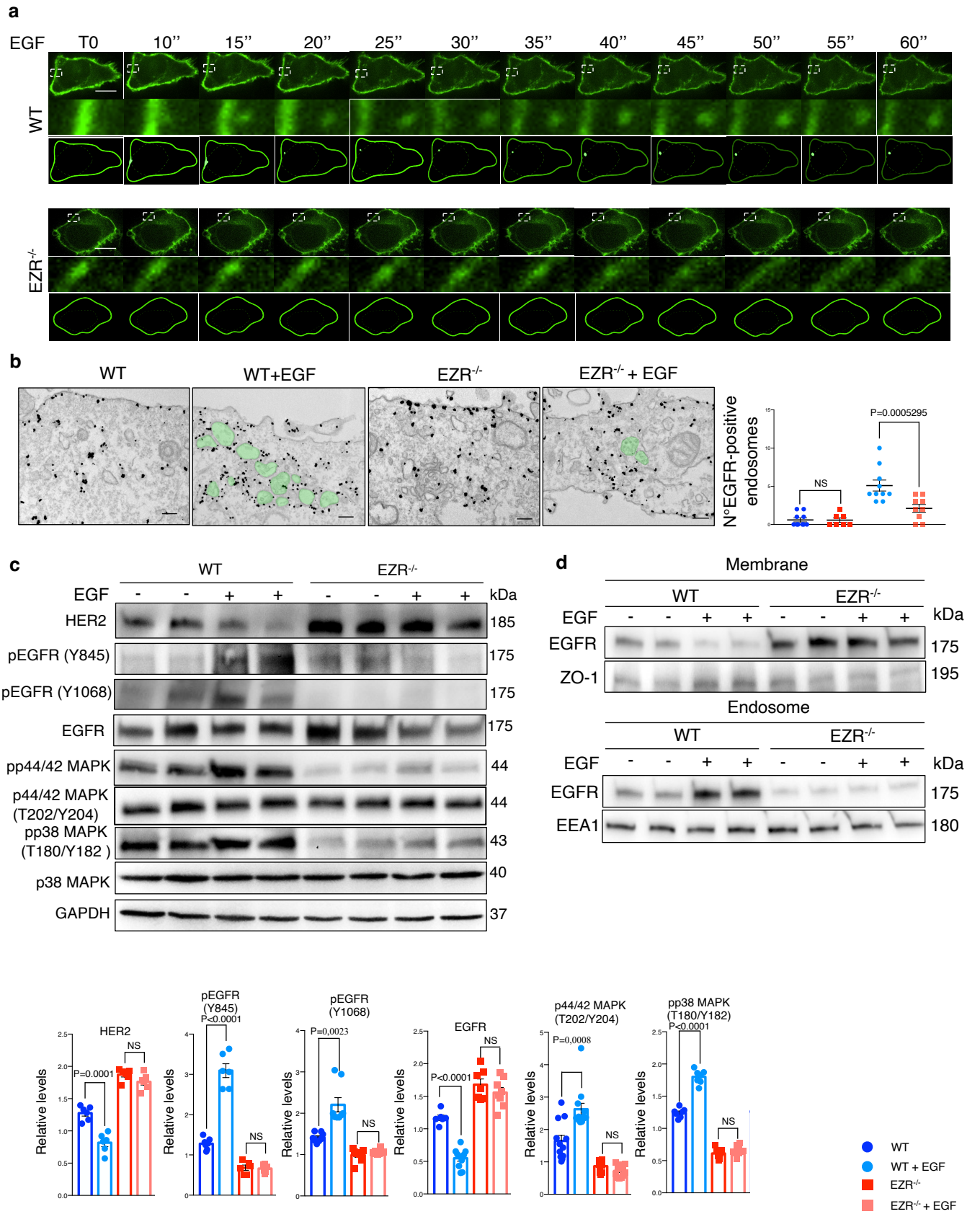
a
EGF
T0
10''
15''
20''
25''
30''
35''
40''
45''
50''
55''
60''
WT
EZR-/-
b
WT
WT+EGF
EZR-/-
EZR-/- + EGF
N°EGFR-positive endosomes
P=0.0005295
NS
c
WT
EZR-/-
EGF
kDa
HER2
185
pEGFR (Y845)
175
pEGFR (Y1068)
175
EGFR
175
pp44/42 MAPK
44
p44/42 MAPK (T202/Y204)
44
pp38 MAPK (T180/Y182)
43
p38 MAPK
40
GAPDH
37
d
Membrane
WT
EZR-/-
EGF
kDa
EGFR
175
ZO-1
195
Endosome
WT
EZR-/-
EGF
kDa
EGFR
175
EEA1
180
HER2
P=0.0001
NS
pEGFR (Y845)
P<0.0001
NS
pEGFR (Y1068)
P=0,0023
NS
EGFR
P<0.0001
NS
p44/42 MAPK (T202/Y204)
P=0,0008
NS
pp38 MAPK (T180/Y182)
P<0.0001
NS
Relative levels
WT
WT + EGF
EZR-/-
EZR-/- + EGF

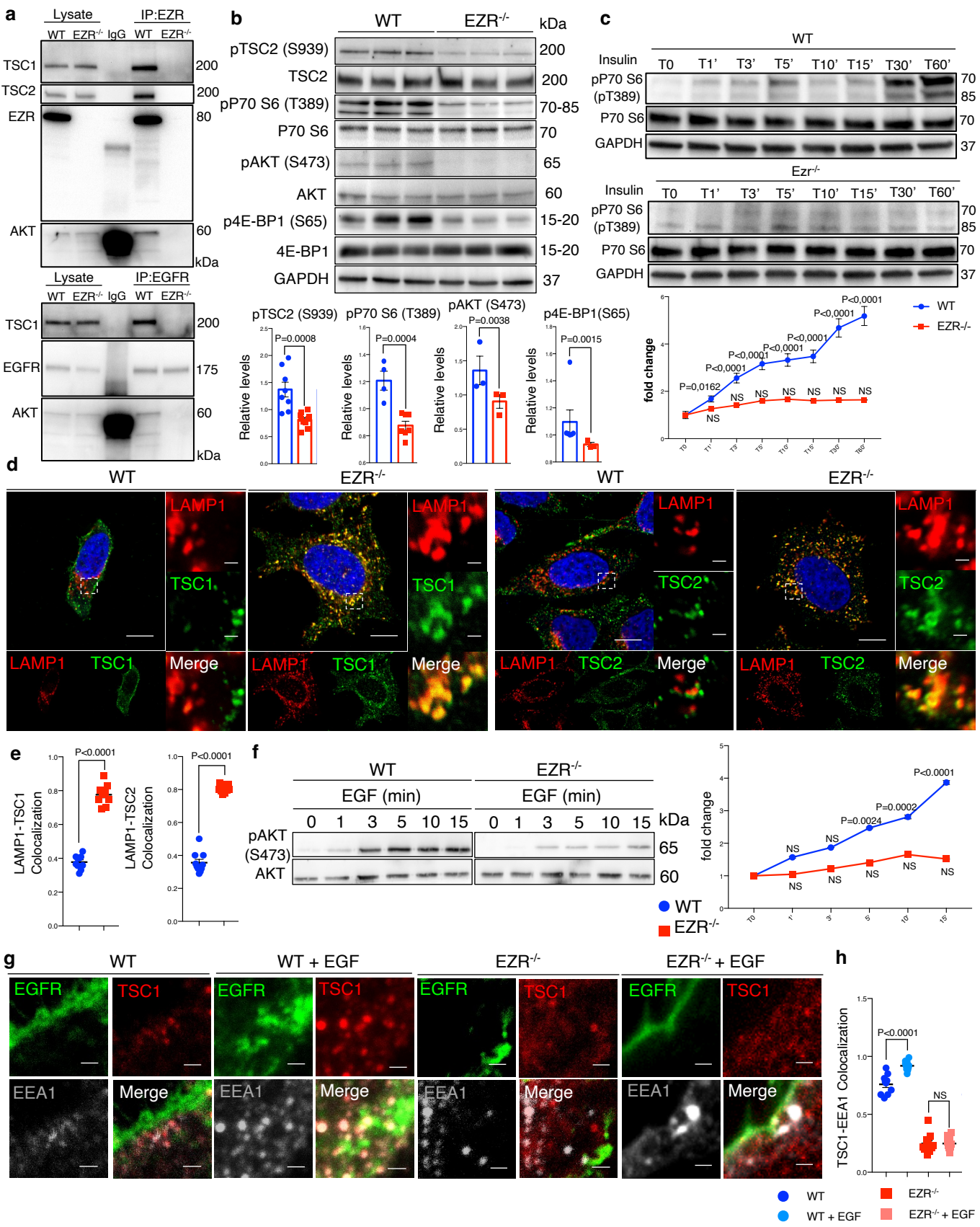
a
Lysate
IP:EZR
WT EZR-/- IgG WT EZR-/-
TSC1
TSC2
EZR
AKT
200
200
80
60
kDa
Lysate
IP:EGFR
WT EZR-/- IgG WT EZR-/-
TSC1
EGFR
AKT
200
175
60
kDa
b
WT
EZR-/-
kDa
pTSC2 (S939)
TSC2
pP70 S6 (T389)
P70 S6
pAKT (S473)
AKT
p4E-BP1 (S65)
4E-BP1
GAPDH
200
200
70-85
70
65
60
15-20
15-20
37
pTSC2 (S939)
P=0.0008
pP70 S6 (T389)
P=0.0004
pAKT (S473)
P=0.0038
p4E-BP1(S65)
P=0.0015
Relative levels
c
WT
Insulin
T0 T1' T3' T5' T10' T15' T30' T60'
pP70 S6 (T389)
P70 S6
GAPDH
70
85
70
37
Ezr-/-
Insulin
T0 T1' T3' T5' T10' T15' T30' T60'
pP70 S6 (T389)
P70 S6
GAPDH
70
85
70
37
fold change
P<0,0001
P<0,0001
P<0,0001
P<0,0001
P<0,0001
P<0,0001
P=0,0162
NS
NS
NS
NS
NS
NS
WT
EZR-/-
d
WT
EZR-/-
WT
EZR-/-
LAMP1
TSC1
LAMP1
TSC1
LAMP1
TSC2
LAMP1
TSC2
LAMP1 TSC1 Merge
LAMP1 TSC1 Merge
LAMP1 TSC2 Merge
LAMP1 TSC2 Merge
e
LAMP1-TSC1 Colocalization
P<0.0001
LAMP1-TSC2 Colocalization
P<0.0001
f
WT
EZR-/-
EGF (min)
EGF (min)
0 1 3 5 10 15 0 1 3 5 10 15 kDa
pAKT (S473)
AKT
65
60
fold change
P<0.0001
P=0.0002
P=0.0024
NS
NS
NS
NS
NS
NS
NS
WT
EZR-/-
g
WT
WT + EGF
EZR-/-
EZR-/- + EGF
EGFR
TSC1
EEA1
Merge
h
TSC1-EEA1 Colocalization
P<0.0001
NS
WT
WT + EGF
EZR-/-
EZR-/- + EGF

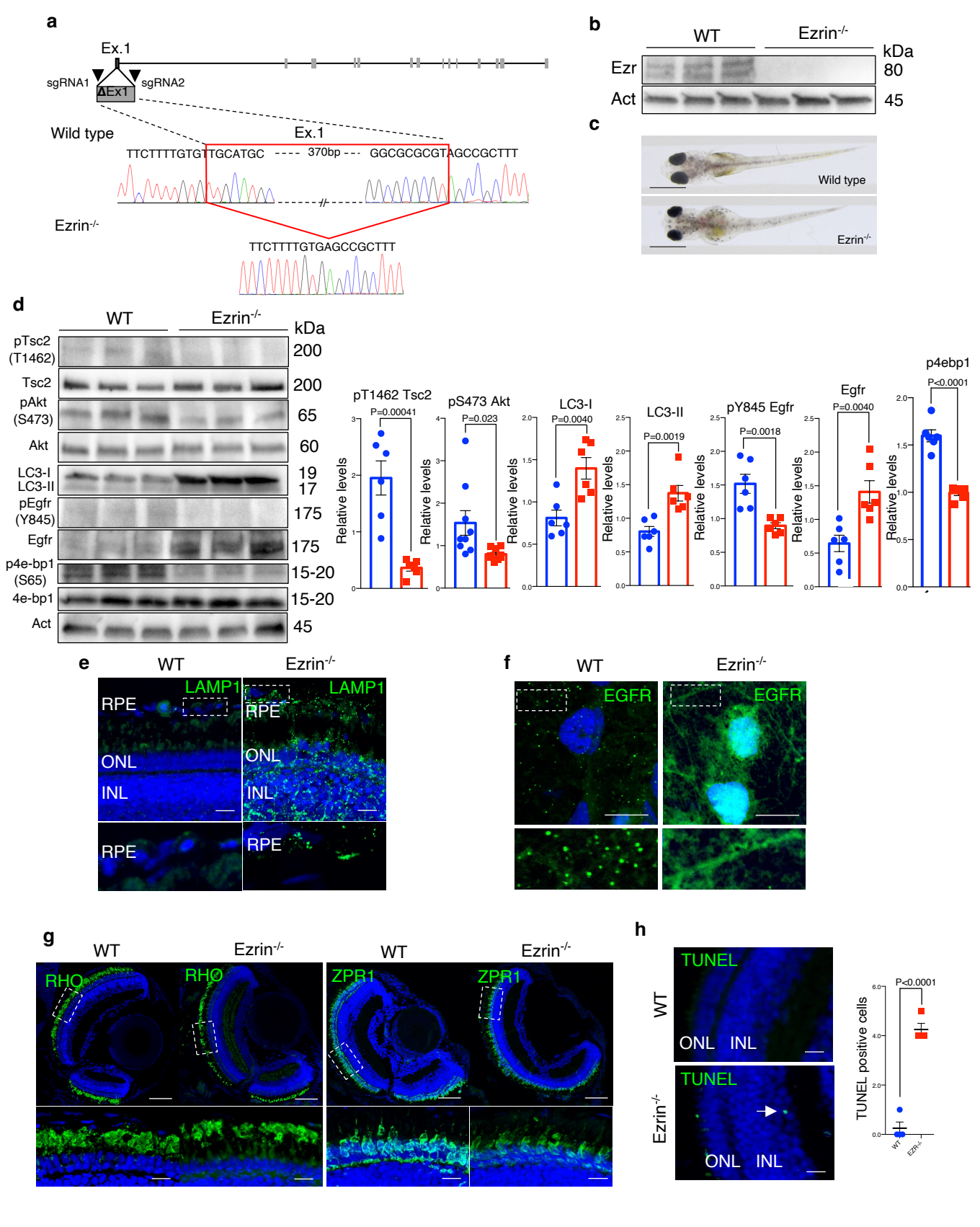
a
Ex.1
sgRNA1
ΔEx1
sgRNA2
Wild type
Ex.1
TTCTTTTGTGTTGCATGC
370bp
GGCGCGCGTAGCCGCTTT
Ezrin-/-
TTCTTTTGTGAGCCGCTTT
b
WT
Ezrin-/-
kDa
Ezr
80
Act
45
c
Wild type
Ezrin-/-
d
WT
Ezrin-/-
kDa
pTsc2 (T1462)
200
Tsc2
200
pAkt (S473)
65
Akt
60
LC3-I
LC3-II
19
17
pEgfr (Y845)
175
Egfr
175
p4e-bp1 (S65)
15-20
4e-bp1
15-20
Act
45
pT1462 Tsc2
P=0.00041
pS473 Akt
P=0.023
LC3-I
P=0.0040
LC3-II
P=0.0019
pY845 Egfr
P=0.0018
Egfr
P=0.0040
p4ebp1
P<0.0001
Relative levels
e
WT
Ezrin-/-
LAMP1
RPE
ONL
INL
f
WT
Ezrin-/-
EGFR
g
WT
Ezrin-/-
WT
Ezrin-/-
RHO
ZPR1
h
TUNEL
WT
Ezrin-/-
ONL
INL
P<0.0001
TUNEL positive cells

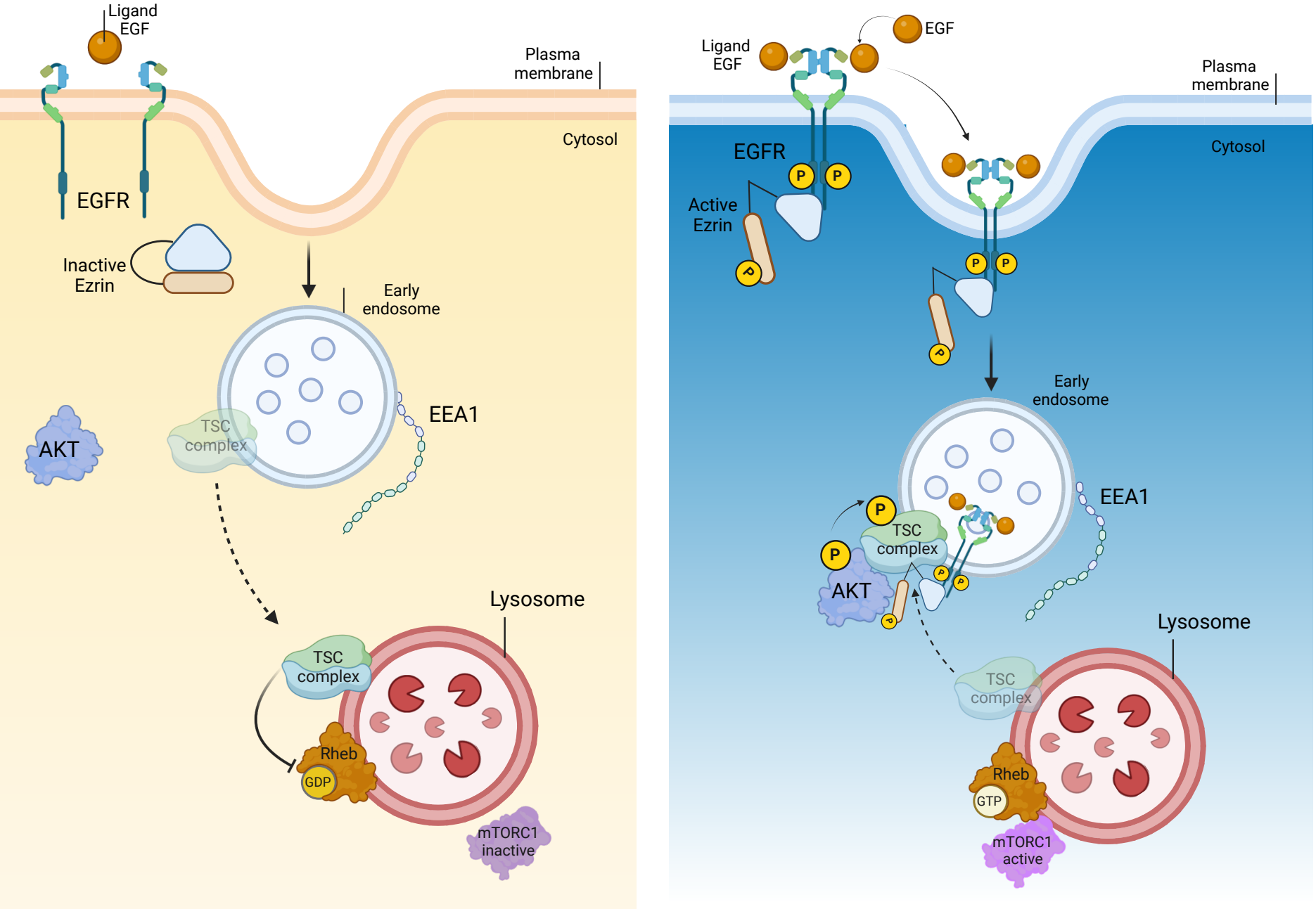
Ligand
EGF
Plasma
membrane
Cytosol
EGFR
Inactive
Ezrin
Early
endosome
EEA1
AKT
TSC
complex
Lysosome
TSC
complex
Rheb
GDP
mTORC1
inactive
EGF
Ligand
EGF
Plasma
membrane
Cytosol
EGFR
P
Active
Ezrin
Early
endosome
EEA1
TSC
complex
AKT
Lysosome
TSC
complex
Rheb
GTP
mTORC1
active